Cell Reports

Resource

High-resolution mapping of cell cycle dynamics during steady-state T cell development and regeneration *in vivo*

Graphical abstract

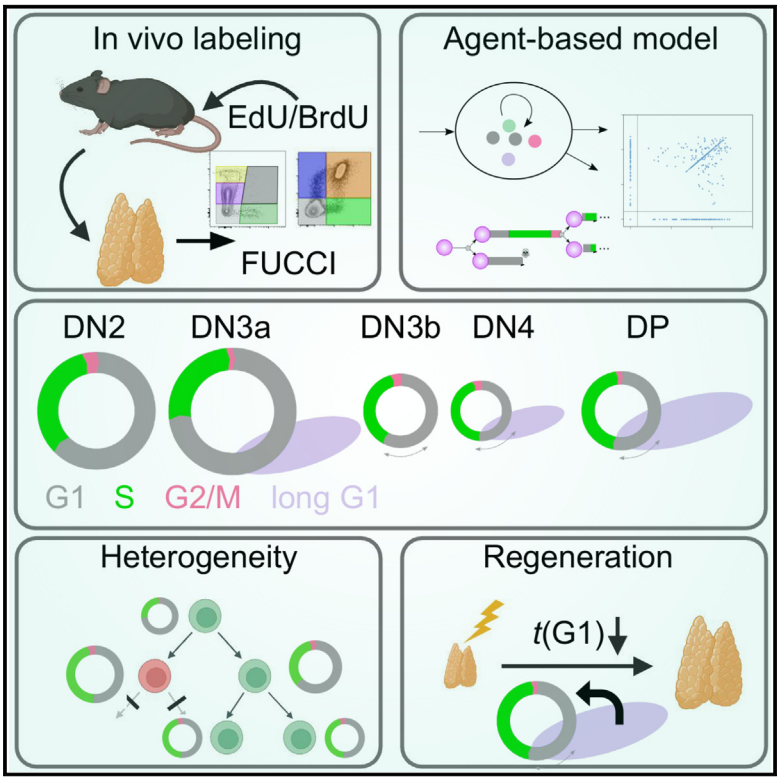

Authors

Heike Kunze-Schumacher, Nikita A. Verheyden, Zoe Grewers, Michael Meyer-Hermann, Victor Greiff, Philippe A. Robert, Andreas Krueger

Correspondence

philippe.robert@ens-lyon.org (P.A.R.), andreas.krueger@immu.bio.uni-giessen.de (A.K.)

In brief

Kunze-Schumacher et al. have developed an experimental and computational framework to generate a quantitative high-resolution map of cell cycle phase durations during murine T cell development. This map provides insight into how cell cycle phases are adjusted between slow- and fast-dividing populations at steady state and in a preclinical model of thymus regeneration.

Highlights

- A framework to quantitatively determine cell cycle phase duration *in vivo*
- A stretch model explains steady-state thymocyte cell cycle speed transitions
- Thymocyte cell cycle phase progression is heterogeneous
- Cell cycle re-entry and G1 shortening promote thymus regeneration

Kunze-Schumacher et al., 2025, Cell Reports *44*, 115132
January 28, 2025
https://doi.org/10.1016/j.celrep.2024.115132

CellPress

Cell Reports

CellPress
OPEN ACCESS

Resource

High-resolution mapping of cell cycle dynamics during steady-state T cell development and regeneration *in vivo*

Heike Kunze-Schumacher,[1] Nikita A. Verheyden,[1] Zoe Grewers,[2] Michael Meyer-Hermann,[3] Victor Greiff,[4] Philippe A. Robert,[4,5,6,*] and Andreas Krueger[1,5,7,*]

[1]Molecular Immunology, Justus-Liebig-University Giessen, 35392 Giessen, Germany
[2]Institute for Molecular Medicine, Goethe University Frankfurt, 60590 Frankfurt am Main, Germany
[3]Department of Systems Immunology and Braunschweig Integrated Centre of Systems Biology (BRICS), Helmholtz Centre for Infection Research (HZI), 38106 Braunschweig, Germany
[4]Department of Immunology, University of Oslo, 0372 Oslo, Norway
[5]Senior author
[6]Present address: Translational Immunology, Department of Biomedicine, University of Basel, Basel, Switzerland
[7]Lead contact
*Correspondence: philippe.robert@ens-lyon.org (P.A.R.), andreas.krueger@immu.bio.uni-giessen.de (A.K.)
https://doi.org/10.1016/j.celrep.2024.115132

SUMMARY

Control of cell proliferation is critical for the lymphocyte life cycle. However, little is known about how stage-specific alterations in cell cycle behavior drive proliferation dynamics during T cell development. Here, we employed *in vivo* dual-nucleoside pulse labeling combined with the determination of DNA replication over time as well as fluorescent ubiquitination-based cell cycle indicator mice to establish a quantitative high-resolution map of cell cycle kinetics of thymocytes. We developed an agent-based mathematical model of T cell developmental dynamics. To generate the capacity for proliferative bursts, cell cycle acceleration followed a "stretch model" characterized by the simultaneous and proportional contraction of both G1 and S phases. Analysis of cell cycle phase dynamics during regeneration showed tailored adjustments of cell cycle phase dynamics. Taken together, our results highlight intrathymic cell cycle regulation as an adjustable system to maintain physiologic tissue homeostasis and foster our understanding of dysregulation of the T cell developmental program.

INTRODUCTION

Control of cell division is pivotal for the development and function of the adaptive immune system. Effective B cell responses in the germinal center, as well as cytotoxic T cell responses, rely on rapid and massive clonal expansion of activated antigen-specific clones, which is mediated through alterations of the cell cycle.[1–3] However, substantially less is known about cell cycle control during developmentally programmed proliferation of lymphocytes.

The thymus produces naive T cells with a diverse T cell receptor (TCR) to fuel the adaptive immune system over extended periods of life. To produce and select such a repertoire, a large number of selectable precursor cells are generated during the course of T cell development. Accordingly, it is characterized by a defined sequence of differentiation events interspersed by proliferative bursts. At steady state, the thymus is periodically colonized by bone marrow (BM)-derived thymus seeding progenitors (TSPs) filling a small number of niches.[4–6] TSPs give rise to early T lineage progenitors (ETPs), the most immature among CD4 and CD8 double-negative (DN) thymocytes.[7,8] ETPs progressively lose multi-lineage potential until T lineage commitment is completed at the DN2b stage.[9–11] Subsequently, thymocytes rearrange their *Trb*, *Trg*, and *Trd* loci to produce pre-TCRs or γδTCRs. Thymocytes expressing a pre-TCR enter the αβT cell lineage marked by β-selection and transition from the DN3a to the DN3b stage. Following upregulation of the CD4 and CD8 co-receptors, double-positive (DP) thymocytes rearrange their *Tra* loci and undergo positive and negative selection to eliminate clones with signaling-incompetent or potentially autoreactive TCRs.

Studies on the turnover of thymocytes *in vivo* have determined the average residence time of thymocytes within phenotypically distinct populations[12–14] and provided estimates of the number of cell divisions within populations.[15,16] After colonization, approximately 160 TSPs give rise to a population of 20,000 ETPs and 25,000 DN2 cells over a period of up to 14 days.[4,13,17] DN2 cells rapidly expand before proliferation ceases in DN3a cells to allow for TCR gene rearrangement. Proliferation then resumes after β-selection. At this stage, population size increases several hundred-fold to generate a sufficiently large pool of precursors for *Tra* rearrangement and subsequent selection events, which are accompanied by substantial amounts of cell death.[18]

The exact nature of how thymocytes adjust cell cycle length in a developmentally controlled manner or as a consequence of instructive signals, such as pre-TCR signaling, remains unclear. In order to better understand cell cycle dynamics in developing thymocytes at steady state and upon perturbation, we sought to generate a high-resolution map of cell cycle phase duration *in vivo*. We employed cell cycle indicator transgenic mice and dual-nucleoside pulse labeling combined with the determination of DNA replication over time. The latter approach allowed us to discriminate cells almost immediately after entry into the S phase as well as just prior to exit of the S phase, generating two virtually synchronized subsets within each thymocyte population. High-resolution data helped to establish a broadly applicable agent-based mathematical model (ABM) for cell cycle analysis, taking into account heterogeneous cell cycle phases as well as *bona fide* non-cycling cells. We extracted the duration of all phases and assigned heterogeneous behavior to distinct cell cycle phases. Finally, we applied our method to a model of thymus regeneration.

RESULTS

Single-nucleoside pulse labeling and cell cycle reporter mice reveal composition and heterogeneity of cell cycle stages in thymocyte populations

We employed BrdU single-pulse labeling combined with DNA content analysis to determine the steady-state proportions of murine thymocytes at distinct cell cycle states (Figures 1A and 1B). In all subpopulations, most cells were in the G0/G1 phase ($BrdU^-$, 2N DNA), and a small fraction of cells were in the G2/M phases ($BrdU^-$, 4N DNA) (Figure 1C). The largest proportions of DNA-replicating cells (S phase, $BrdU^+$ and 2N < DNA content < 4N) were found in the DN2, DN3b, and DN4 subsets (Figure 1C), whereas the lowest proportions were found in DN3a and pre-selection DP cells as well as post-selection DP and SP thymocytes (Figure 1C).

Next, we analyzed a transgenic mouse model with fluorescent reporters linked to cell cycle progression (fluorescent ubiquitylation-based cell cycle indicator [FUCCI] mice).[19] These mice express a green fluorescent reporter (monomeric Azami Green; mAG) during the S phase and increasing levels of a red fluorescent reporter (monomeric Kusabira Orange 2; mKO2) through the course of the G1 phase, hence providing qualitative information on G1 phase duration and quiescence.[19] Frequencies of mAG-labeled thymocytes correlated well with S-phase frequencies determined by a single BrdU pulse and DNA content analysis, indicating the faithful reporting of cell cycle stages in the FUCCI system (Figures 1D and 1E). Thymocytes outside the S phase (mAG^-) were subdivided into G2/M/early G1 ($G1^{early}$), intermediate G1 ($G1^{int}$), and late G1/G0 based on increasing levels of mKO2. Thymocytes contained between 20% and 40% of cells in $G1^{int}$ from ETPs to DN3a, while DN3b and DN4 subsets showed lower amounts of $G1^{int}$ cells, with 3% and 15%, respectively, indicating shorter G1 phases in DN3b and DN4. Thus, FUCCI reporter expression suggests that rapidly cycling DN3b and DN4 thymocytes contain higher frequencies of cells in the S phase and a shorter G1 phase (Figures 1D and 1E). Post-selection thymocytes progressively acquired high and discrete levels of mKO2, suggesting that these cells ultimately exit from the cell cycle on the path of maturation toward naive T cells (Figures 1D and 1E). Taken together, the results of the steady-state analysis confirmed previously established switches between non-proliferative and proliferative phases of T cell development.

Dual-nucleoside pulse labeling reveals rates of entry in S phase

Next, we employed dual-nucleoside pulse labeling to study dynamic cell cycle behavior. Cells were sequentially labeled *in vivo* with EdU and BrdU 1 h apart, followed by analysis 1 h after the second pulse (Figure 2A). The window of action of EdU or BrdU labeling above the detection threshold has been estimated to be 45–60 min after label administration, with EdU displaying a somewhat shorter bioavailability than BrdU.[20] Thus, labeling at a 1-h interval creates single-nucleoside-positive EdU^+BrdU^- and EdU^-BrdU^+ populations, representing cells that ceased DNA replication within 1 h after label administration (post-S) and cells that initiated DNA replication within less than 1 h after BrdU administration (early S), respectively (Figure 2B). Accordingly, single-nucleoside-positive populations provide information on the rates of entry into and exit from the S phase.

Analysis of EdU^-BrdU^+ thymocytes showed that DN2, DN3b, and DN4 had frequencies of S-phase entry of 5%–7% in <1 h (Figure 2C). DN1, DN3a, and pre-selection DP cells had frequencies of S-phase entry around 2% in <1 h, and those of post-selection DP and CD8SP cells were even lower (Figure 2C). Virtually no CD4SP cells started DNA replication within this time frame (Figure 2F). Altogether, the results show that the frequency of thymocytes starting DNA replication corresponds well with the steady-state analysis (Figure 1C).

Frequencies of EdU^+BrdU^- cells, corresponding to cells exiting the S phase during the labeling process, were comparable to those of EdU^-BrdU^+ thymocytes but somewhat higher throughout (Figures 2D and 2E), which might be due to small differences in the bioavailability of both nucleoside analogs and nonlinear kinetics of DNA replication in certain populations. Assuming that all cells are cycling and have identical phase durations within a population, the rate of S-phase entry, i.e., the percentage of cells entering the S phase in 1 h, informs on how many hours are necessary for 100% of the initial cells to enter the S phase and therefore provides an estimate of the full cycle (Figure 2C). Under this assumption, DN2, DN3b, and DN4 cells completed one full cycle within 12, 8, and 9.5 h, respectively. DN1, DN3a, and pre-selection DP harbored average cell cycle durations of 47, 36, and 34 h, respectively. Post-selection DP and CD4SP thymocytes had estimated cell cycle durations that extended well beyond their estimated lifetimes. CD8SPs were estimated to cycle in 52 h, consistent with their progression to quiescence. Therefore, the rate of S-phase entry cannot be directly translated into cell cycle duration due to the presence of quiescent cells.[17]

Taken together, the results of single-pulse and dual-pulse nucleoside labeling revealed substantial differences between thymocyte populations with slow and rapid turnover, consistent with previous studies.[15] They also provided initial quantitative information about the total cell cycle duration based on the determination of the rate of cells starting DNA replication and qualitative information on the relative contribution of the S phase to the cell cycle.

CellPress
OPEN ACCESS

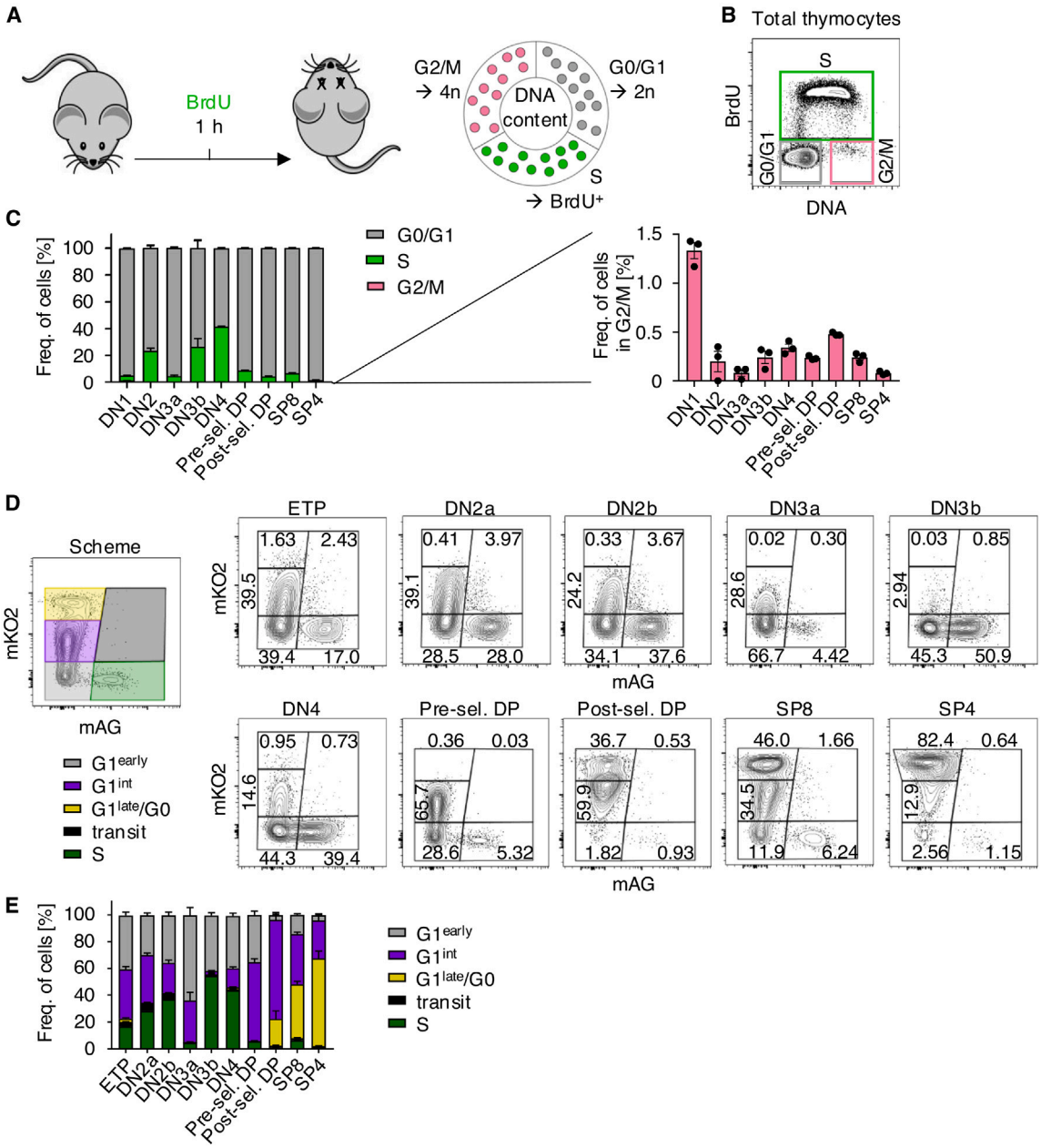

Figure 1. Single-nucleoside pulse labeling and cell cycle-reporter mice reveal composition and heterogeneity of cell cycle-stages in thymocyte populations

(A) Schematic representation of the performed experiments.

(B) Flow cytometric gating strategy to identify G0/G1, S, or G2/M phase.

(C) Frequencies of cells in G0/G1, S, or G2/M phase of WT thymocytes. Data are represented as mean ± SEM. $n = 3$ mice.

(D) FUCCI gating strategy and profiles of thymocytes. $G1^{early}$: gray, $mAG^{-}mKO2^{-}$; $G1^{int}$: purple, $mAG^{-}mKO2^{+}$; $G1^{late}$/G0: yellow, $mAG^{-}mKO2^{++}$; transit: black, $mAG^{+}mKO2^{+}$; S: green, $mAG^{+}mKO2^{-}$.

(E) Frequencies of FUCCI cell subsets as defined in (D). Data are represented as mean ± SEM. $n = 6$ mice.

High-resolution tracking of virtually synchronized cells using dual-pulse labeling combined with DNA content analysis over time informs on the duration of individual cycle phases

Next, we sought to quantitatively determine the duration of cell cycle stages in each thymocyte subset. Dual-nucleoside pulse labeling 1 h apart as described above creates virtually synchronized populations at the start of the S phase ($EdU^{-}BrdU^{+}$) and at its end ($EdU^{+}BrdU^{-}$). DNA content analysis was performed to trace S-phase progression of virtually synchronized cells from 1 to 20 h post-BrdU injection (Figure 3A). Due to limitations in cell numbers and few nucleoside

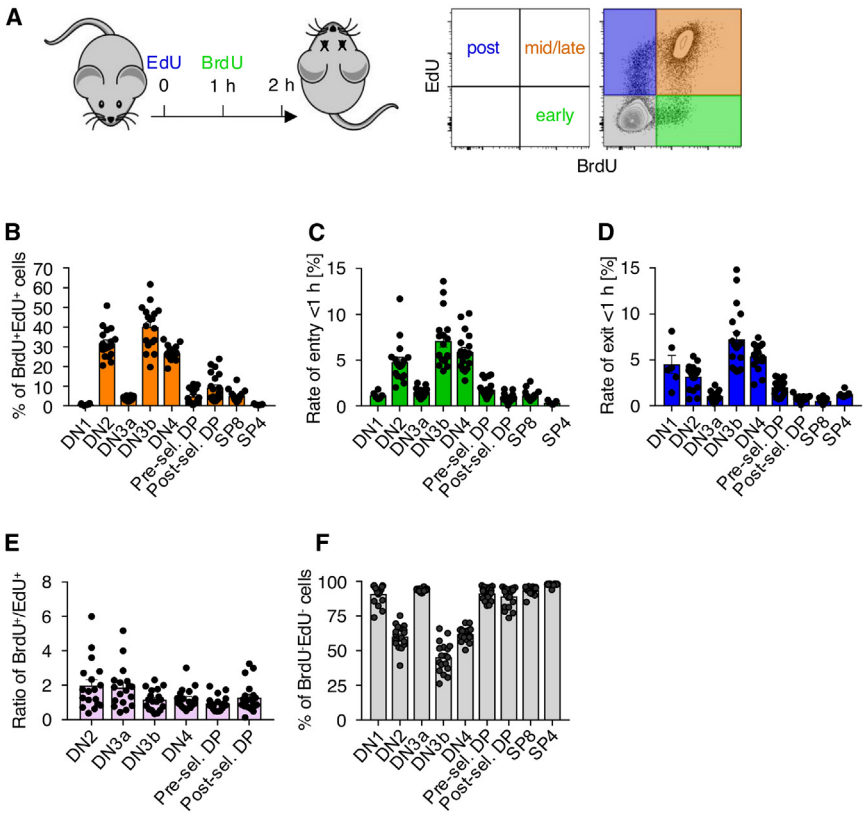

Figure 2. Dual-nucleoside pulse labeling reveals rates of S-phase entry

(A) Schematic overview and representative flow cytometric gating strategy. Mice received consecutive pulses of EdU and BrdU 1 h apart. Analyses were performed 1 h after the second pulse. Thymocytes in the S phase during both pulses are EdU$^+$BrdU$^+$ (orange, mid/late-S phase). EdU or BrdU single-positive thymocytes represent cells that have ceased DNA replication and left the S phase (EdU$^+$, blue, post-S phase) or newly entered the S phase during the second pulse (BrdU$^+$, green, early S phase), respectively.

(B–F) Graphs show frequencies of EdU$^+$BrdU$^+$ cells (B), EdU$^-$BrdU$^+$ cells (C), and EdU$^+$BrdU$^-$ cells (D) and ratios of BrdU$^+$/EdU$^+$ cells (E) and EdU$^-$BrdU$^-$ cells (F). Data are represented as mean ± SEM. n = 6–20 mice of two independent experiments.

incorporating cells, DN1 and both SP subsets were omitted from this analysis.

The dynamics of DNA incorporation of cells that started (green), left (blue), or stayed (orange) in the S phase during the interval of the first labeling is shown for representative slow- and fast-proliferating populations, DN3a and DN4, respectively (Figures 3B and S1A).

We determined the S-phase duration in virtually synchronized cells at S-phase entry (EdU$^-$BrdU$^+$, green) and non-synchronized cells (EdU$^+$BrdU$^+$, orange) by monitoring the increase of DNA content from 2N to 4N toward a complete round of DNA duplication (Figures 3C and S1B).[21] We determined S phases of 6–7 h for DN3b and DN4 cells (Figure 3C). Longer S-phase durations of 8–9.5 h were observed for DN2, DN3a, and pre-selection DP cells, although DN2 cells displayed higher rates of cell cycle entry compared to DN3a and DP and were therefore cycling substantially faster than the latter two populations (Figure 2C). These data suggest that S-phase shortening below a certain limit is a feature restricted to extremely fast-proliferating DN3b and DN4 subsets. Post-selection DP cells contained more DNA already at the early time points of analysis, and cells remained in the S phase for considerably longer than other populations. The underlying mechanism of this peculiarity remains unknown.

Virtually synchronized cells at S-phase exit (EdU$^+$BrdU$^-$) had mostly reached G1 already at the 1 h time point of analysis, corresponding to 1.25–1.5 h after exiting the S phase if we include a delay of labeling bioavailability (Figures 3B and S1A, blue histograms). We conclude that for all analyzed thymocyte populations, the G2/M duration is less than 1.5 h. Pre-selection and post-selection DP cells had somewhat higher frequencies of cells remaining in G2/M at this point in time, suggesting that the distribution of G2/M may be broader or that the transition between the S and G2/M phases is prolonged (Figure S1A). The G1-phase duration can be derived from determining the time point of the onset of DNA replication (DNA content >2N) of cells virtually synchronized at S-phase exit (Figures 3B and S1A, blue histograms). DN3b and DN4 populations displayed minimal G1-phase durations of 3.1 and 2.8 h, respectively (Figure 3D). DN3a and pre-selection DP cells had minimal G1-phase durations of 5.25 and 5.1 h, respectively (Figure 3D). Surprisingly, the G1-phase duration in DN2 cells extended beyond this type of analysis. DNA content analysis after 16 and 20 h revealed plateaus of DNA content at approximately 50% for DN4 and post-selection DP cells and 30% for pre-selection DP cells. If the G1 duration is heterogeneous between cells, then this approach may focus on cells with the shortest G1 duration and underestimate the population average. Apparent stable frequencies of G1 cells at later time points can be explained by the de-synchronization of cell cycles over extended periods of time, transitions to the subsequent developmental stage, or both.

We tested whether label-negative cells provided some indication of population heterogeneity. Cell cycle entry in at least some label-negative cells was detected already at 2 h in fast-cycling populations (DN3b and DN4) and at 4 h in DN2 cells. In contrast, no cell cycle entry was observed in pre-selection DP cells, consistent with these cells ceasing proliferation in order to start TCR gene rearrangements (Figure S2).

Taken together, the results of a combination of dual-pulse labeling with analysis of temporally resolved DNA replication provided a direct estimate on the duration of individual cell cycle phases for thymocytes assuming population homogeneity (Figure 3E).

CellPress
OPEN ACCESS

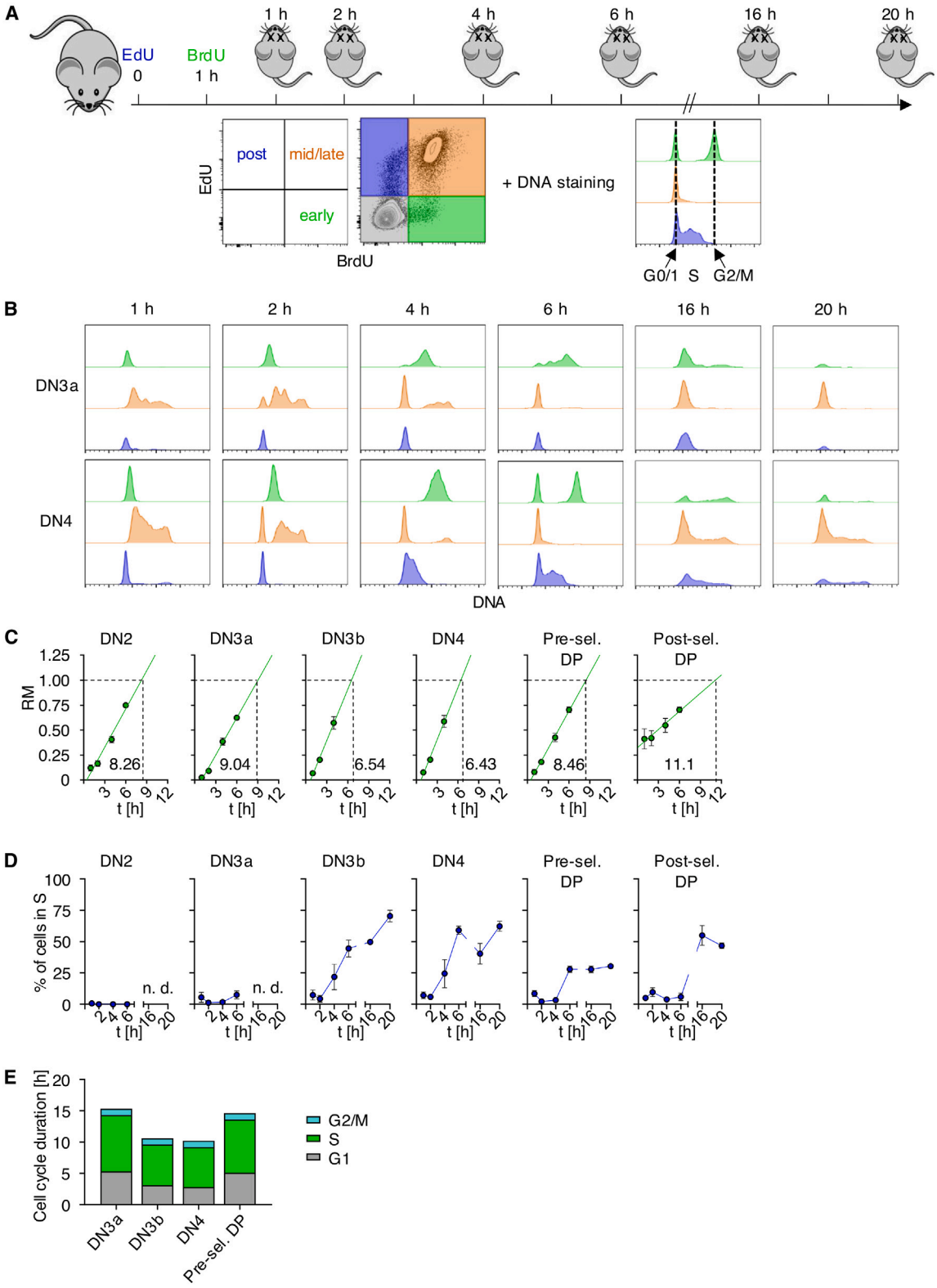

(legend on next page)

Modeling thymocyte population dynamics based on high-resolution cell cycle analysis

Partially overlapping information obtained from different experiments allowed us to define boundaries of cell cycle phase durations for most subsets yet also revealed some apparent discrepancies potentially arising from the assumption of homogeneous populations. To accurately estimate the duration and heterogeneity of the cell cycle phases from dual-pulse labeling experiments combined with DNA content analysis, we developed an ABM of cell division and labeling.

In brief, the ABM is inspired by the Cyton model and simulates EdU and BrdU incorporation in a population of cells progressing through G1, S, and a combined G2/M phase, followed by *in silico* gating of EdU^-BrdU^-, EdU^+BrdU^-, EdU^-BrdU^+, and EdU^+BrdU^+ cells (Figure 4A, top).[22] We also created a two-population model, accounting for the inflow of cells from the precursor populations during labeling, to refine the estimates of cell cycle phase durations (Figure 4A, bottom).

In detail, phase durations follow lognormal time distributions whose average and width are to be estimated from experimental data (the unknown parameters). At division, two daughters are created at G1. Times of completion of the G1, S, and G2/M phases are sampled from the respective distributions. A death time is sampled at birth from an exponential time distribution and is triggered if it happens before the end of G2/M. We incorporate a separate pool of cells that are arrested in G1 for a long time, referred to as "long-G1" cells. We reproduce the dual-pulse EdU and BrdU labeling (Figure 4A, center) and gate cells *in silico* according to their EdU and BrdU levels. Cells from each gate are assessed for their cell cycle phase, and a cost is calculated between a simulation and the experimental data (Figure 4A, right). Automated parameter estimation simulates labeling for many possible hypothetical durations of each cell cycle phase and identifies the most likely cell cycle durations by minimizing the cost. To avoid overfitting due to unnecessary model complexity, we devised five different hypotheses comparing the possible heterogeneity of each cell cycle phase within each population (Figure 4B). The simplest hypothesis ("non-variable") assumes a fixed duration of each phase. Intermediate hypotheses ("G1 or S or G2/M variable") consider only one phase to be variable, while the most complex ("all variable") allows each phase to be different. For each population, we performed a parameter estimation 10 independent times on a training dataset comprising the first four analysis time points and compared the quality (cost) of each hypothesis, with or without bystander long-G1 cells. In the DN3b population, the hypotheses "variable G1" and all variable showed lower costs than the other hypotheses (Figures 4B, S3, and S4). Interestingly, the hypothesis "variable S" did not perform better than variable G1 and was inconsistent with the "percentage of EdU^+BrdU^- cells (post) in G1″ and the DNA-labeling dynamics, suggesting that variable S-phase durations are not required to explain the data. The "all variable" hypothesis did not further improve the quality of the curves or the cost. Thus, a variable G1 phase provides the best explanation for the data with minimal model complexity in DN3b cells. Of note, this finding was confirmed in the full validation dataset comprising six analysis time points (Figure S5). The simulation curves with parameters inferred from the training dataset using the "variable G1" hypothesis were largely consistent with the labeling dynamics at the later time points and with the curves obtained when inferring parameters from the full dataset with the variable G1 (Figure S4). Using a profile likelihood analysis, we confirmed that only one set of cell cycle phase durations can explain the experimental dataset. This method fixes different possible durations of one phase and estimates the other ones (Figures 4C and S5C, blue curves). The existence of a minimum cost means that only one value for this phase duration best explains the data (the phase duration is "identifiable"). We conclude that the durations of all three phases are accurately identified by our approach. For the DN3b (Figure 4C), DN4, and pre-selection DPs (Figure S5C), four time points (training dataset, blue curves) were sufficient to identify cell cycle phase durations that were consistent between the training and the full dataset (red curves). However, for the DN2 and DN3a populations, a minimum of six time points was required to identify the G1 duration due to a longer G1 phase, which cannot be fully captured by the initial four time points. Varying the death rate or the number of divisions did not affect the results (Figures S6A and S6B). Therefore, the combined experimental modeling approach is able to identify both phase heterogeneity and duration *in vivo* (Table S1).

To account for the possibility of already-labeled precursor cells entering the simulated population, we developed a two-stage model simulating dual-pulse labeling for both the population of interest (with phase durations to be estimated) and a large pool of its precursor cells using the phase durations previously identified with the one-population model (Figure 4B). This model is extremely slow, which makes identifiability analysis and hypothesis comparison impracticable. The estimated cell cycle durations were similar between both the one-population and two-population models (Figure S6D), demonstrating that the complexity of the two-population model is not required per se to identify cell cycle phase durations but can be used as a refinement that incorporates more biological complexity.

Figure 3. High-resolution tracking of virtually synchronized cells using dual-pulse labeling combined with DNA content analysis over time informs on the duration of individual cycle phases

(A) Schematic overview and representative flow cytometric gating strategy.

(B) Analysis of DNA content of DN3a and DN4 thymocytes over time. Each plot depicts an overlay of the DNA content of EdU^-BrdU^+ (green), EdU^+BrdU^+ (orange), and EdU^+BrdU^- (blue) cells.

(C) Analysis of S-phase duration based on relative movement (RM) of EdU^-BrdU^+ cells (early S phase) through the S phase (see STAR Methods). Green line: linear regression. Numbers adjacent to linear regression: S-phase duration in h derived from linear regression. n = 3–5 mice per time point, 2 independent experiments.

(D) Quantification of S-phase re-entry of EdU^+BrdU^- thymocytes over time. n = 4–5 mice for each time point, 2 independent experiments.

(E) Total cell cycle length and cell cycle phase composition of thymocytes. For DN3a, DN3b, DN4, and pre-selection DP thymocytes, the length of the G1 phase was calculated based on RM values of EdU^+BrdU^- S-phase cells at later time points (dark gray). S-phase length (green) was determined as shown in (C).

CellPress
OPEN ACCESS

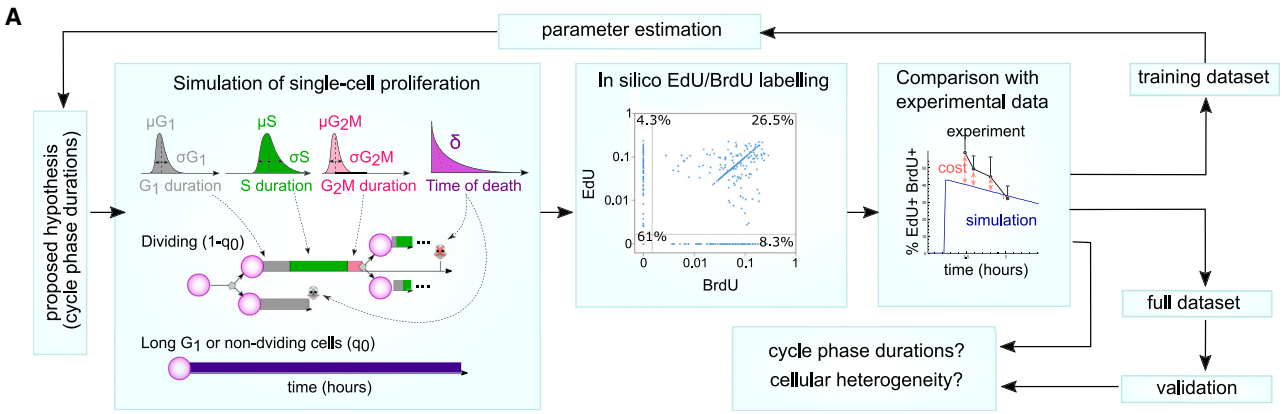

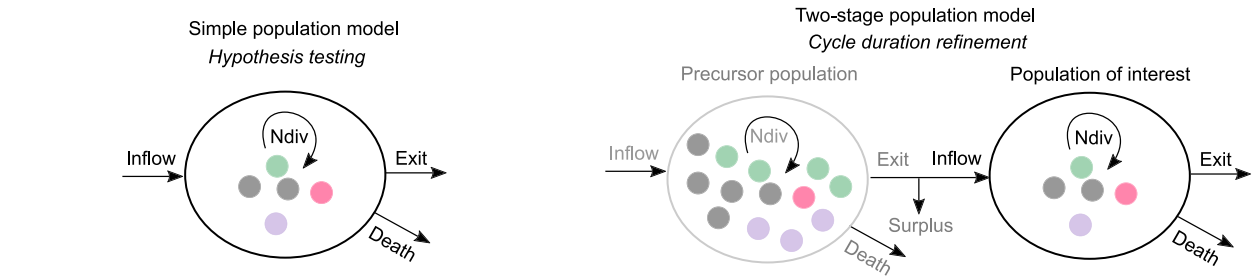

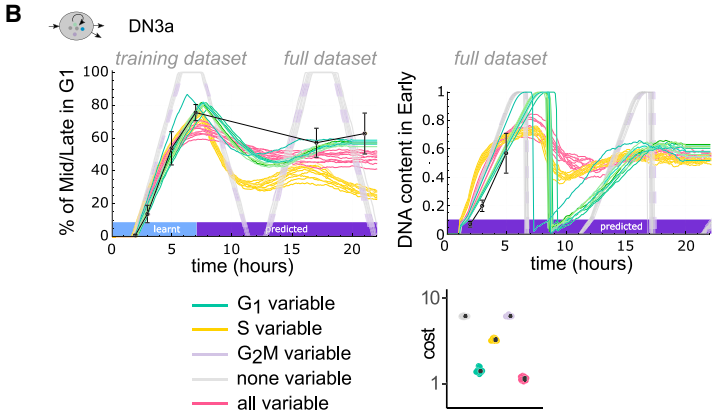

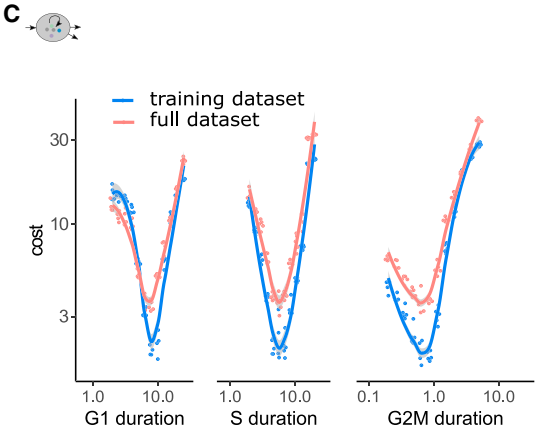

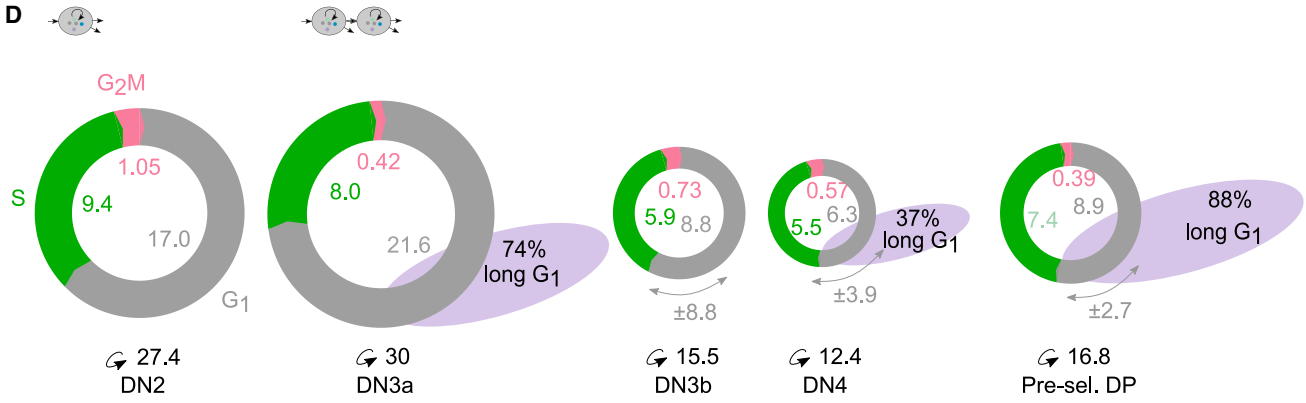

(legend on next page)

Altogether, the results of our combined experimental and computational framework provide a high-resolution map of cell cycle phase durations during T cell development from the DN2 to pre-selection DP stages (Figure 4D; Table S1): the cycle durations ranged between 12.4 h for DN4 to 30 h in the DN3a population. The S phases ranged from between 5.5 h in the DN4 population to 8.8 h in the DN2 population. The DN2 and DN3b datasets could be explained without long-G1 cells. The DN3a population required 74% of long-G1 cells, consistent with the need for TCR rearrangement and β-selection at this stage. The pre-selection DP population was best explained including 88% of long-G1 cells, consistent with proliferation arrest during TCRα gene rearrangement and the onset of thymic selection at this stage. Surprisingly, the DN4 population required ∼37% of long-G1 cells, which was necessary to explain the low re-entry of unlabeled cells into the S phase, suggesting the existence of a subpopulation of cells with different cell cycle kinetics.

Decision to re-enter the S phase after one round of cycling defines cell cycle heterogeneity

To experimentally validate the heterogeneous behavior of cells, we first sorted DN3a thymocytes at defined stages of the cell cycle and differentiated them *in vitro* on OP9-DL1 co-cultures (Figure 5A). FUCCI^{-} (corresponding to G1^{early}) cells progressively acquired mKO2 fluorescence over time, in line with prolonged time spent in G1 (Figures 5B and 5C). A subset of cells (2%–4%) in the S phase (mAG^{+}) was detected already after 2 h of culture, and the frequency of this population remained virtually constant throughout the period of culture, suggesting that this population is not continually fueled by cells from the mid/late-G1 phase. Sorted mKO2^{+} cells (mid/late G1) gave rise to a larger proportion of S-phase cells over time when compared to G1^{early} cells, increasing over a period of 12 h but remaining constant thereafter (Figure 5D). G1^{early} cells appeared after 14–16 h of culture, consistent with the S-phase duration of 7.5–9 h determined *in vivo*, and reached a plateau after 20 h. Starting from sorted mAG^{+} (S-phase) cells, the frequencies of G1^{early} cells steadily increased between 2 and 12 h, followed by an expansion of G1^{int} cells, indicating that G1^{int} cells emerge from FUCCI^{-} cells after approximately 10 h (Figure 5E). In contrast, no *de novo* increase in S-phase cells was observed during the culture period. Taken together, these data indicate that the transition from the S phase through division into G1 is kinetically fixed, whereas re-entry into the S phase is independent from a predetermined G1-phase duration.

Next, we re-analyzed virtually synchronized thymocytes from dual-pulse labeling experiments for evidence of intra-population heterogeneity. Experiments described above allowed us to faithfully quantitate the duration of one round of cycling but did not provide information about multiple division cycles. We analyzed the onset of a second round of DNA replication in virtually synchronized fast-cycling DN3b and DN4 cells at S-phase exit (Figure 5F). Both populations displayed a bimodal distribution of DNA amounts detectable at 4–5 h after completion of the previous S phase. Whereas approximately 70% and 60% of DN3b and DN4 cells, respectively, had completed G1 and re-initiated DNA replication at that time point, the remainder of the cells were in the G1 phase. Of note, this bimodal distribution remained essentially constant for at least an additional 2 h.

Taken together, *in vitro* and *in vivo* data validated the cell cycle heterogeneity predicted by our mathematical model and showed that, at least for DN3b and DN4 cells, this heterogeneity predominantly manifests itself prior to or at the G1-to-S-phase transition.

Population-specific cell cycle phase alterations determine thymus regeneration

To test whether the combined experimental and computational framework of high-resolution quantification of cell cycle dynamics was broadly applicable, we analyzed perturbation-induced alterations of cell cycle dynamics. The restoration of thymus size after pre-conditioning constitutes a major bottleneck for regeneration of the immune system after hematopoietic stem cell transplantation.[23] We determined cell cycle dynamics during the regeneration of thymus size at 6 days after sublethal irradiation, when thymus cellularity is in the process of recovery after a maximal depletion at around day 4 after irradiation.[24,25] At 6 days after irradiation, thymus cellularity is typically at around 10% of its original size, but most populations have recovered to at least 50% of their steady-state frequencies to permit analysis[24,26] (Figures 6A and S7A). First, we performed dual-pulse labeling. At 6 days post-irradiation, all populations, with the exception of DN3a cells, displayed substantial frequencies of cells in the S phase, ranging from 27% to 69% (Figure 6B). When compared to the corresponding populations in non-manipulated mice, DN2 and DN3a cells had 1.5- to 2.5-fold higher frequencies in the S phase, whereas these frequencies were unaltered in DN3b and DN4 cells (Figure 6B). Both subsets of DP thymocytes displayed a 4.6- to 26-fold increase of S-phase cells. Entry rates into the S phase during regeneration were similar in DN2 and DN3b cells, when compared to steady state, but markedly increased in DN3a, DN4, and pre-selection DP thymocytes, indicating shorter overall cell cycle durations in these populations (Figure 6C). We

Figure 4. Modeling thymocyte population dynamics based on high-resolution cell cycle analysis

(A) Workflow for phase duration inference. Left: agent-based mathematical model (ABM) for cell cycle progression using lognormal time distributions for phase durations and constant death rate. Long-G1 cells: fraction of bystander cells. Middle: *in silico* single-cell profiles for EdU and BrdU labeling. Right: a cost (likelihood) evaluates the quality of a simulation compared to the data. Parameter estimation algorithms iteratively find the cell cycle durations that best explain the data. Bottom: one-population ABM used for hypothesis comparison and two-population ABM used for refined estimations of cycling speed.

(B) Comparison of data (black) and simulations (colored) curves under different cell cycle heterogeneity hypotheses for the DN3b population. 10 independent fittings for each hypothesis are shown. Light blue: training datapoints (“learnt”), dark blue: validation datapoints (“predicted”). Error bars represent the SD of experimental datapoints (n = 6).

(C) Identifiability analysis of phase durations by profile likelihood in DN3b. y axis: cost of the simulations; x axis: fixed value of one cycle phase duration. Other cycle phases are estimated. Blue: training dataset only; red: training and test datasets.

(D) Cell cycle phase durations (in hours) identified using the full dataset, with the one-population model for DN2 and the two-population model for downstream populations. Gray: percentage of long-G1 cells. Arrows: estimated variation of the G1 phase between cells.

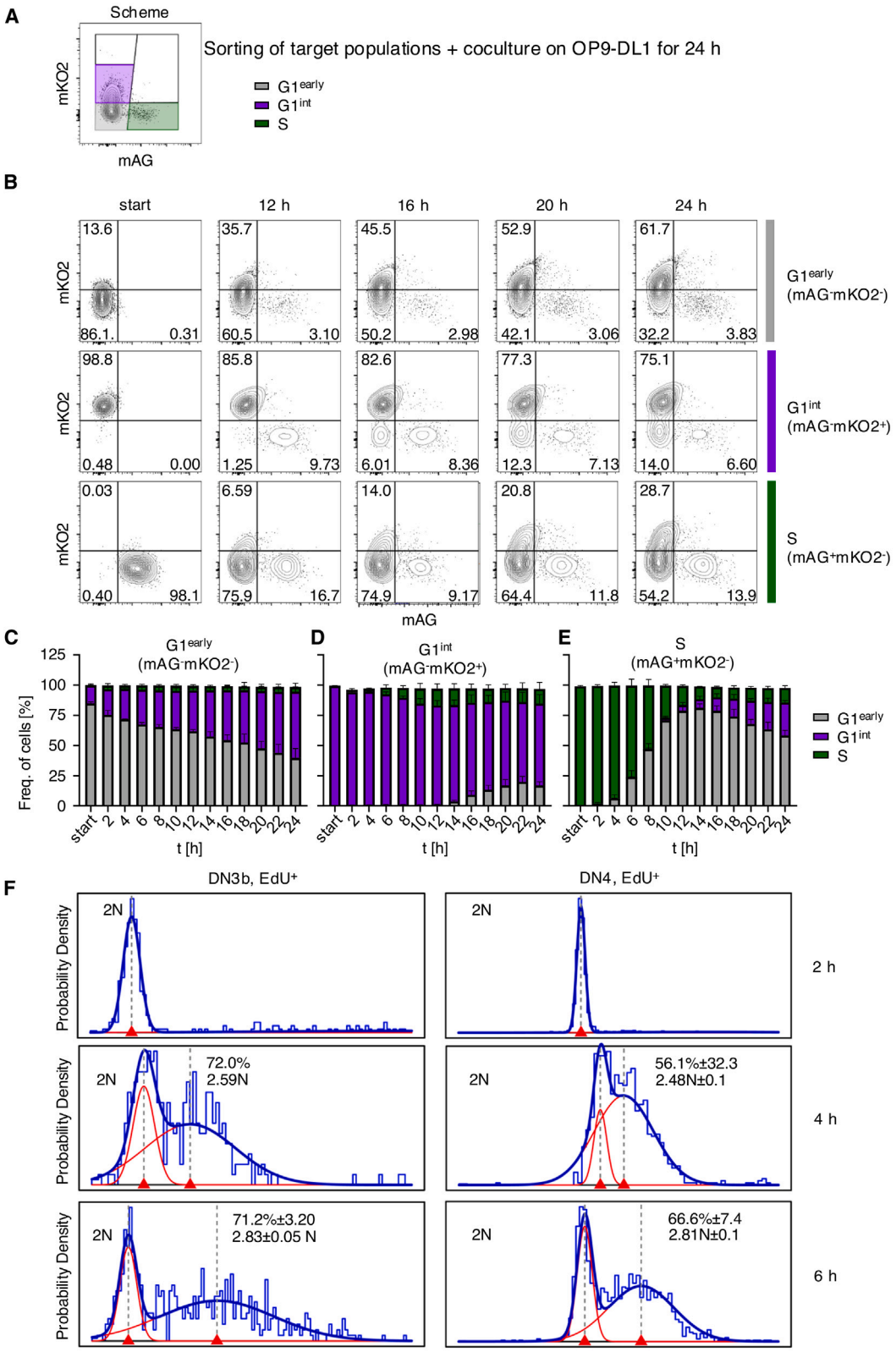

(legend on next page)

noted that during regeneration, S-phase exit rates were mostly smaller than entry rates (Figure 6D). Taken together, dual-pulse labeling revealed a complex pattern of alterations in cell cycle progression with a notable uncoupling of S-phase entry and exit. Lower exit rates are consistent with an overall increase in cells residing in the S phase during regeneration. These observations underscore that S-phase frequencies, commonly used as a marker for proliferation at steady state, only partially reflect proliferation speed.

Next, we analyzed dynamic cell cycle behavior *in vivo* using the previously established dual-pulse labeling approach in conjunction with DNA labeling. Estimated S-phase lengths in DN2 and DN3a thymocytes were similar, with a trend toward a longer duration during regeneration when compared to the steady state (Figure 6E). In DN3b, DN4, and pre-selection thymocytes, the S-phase duration was approximately 45 min longer upon regeneration. Thus, despite overall reduced cycling times, the S-phase duration is increased in a model of post-irradiation thymus regeneration. Frequencies of single labeled cells within the post-selection DP subset were too low for a robust quantitative analysis. Next, we applied the ABM described above to extract alterations in cycling behavior at the individual stage level. Mathematical modeling revealed shorter overall cell cycle durations for DN2, DN3a, DN4, and pre-selection DP cells upon regeneration, with the DN4 cell cycle duration being close to the steady-state situation (Figure 6F). The cell cycle length of DN3b was unaltered in regenerating thymi when compared to the steady state. Decreases in cell cycle length could be completely attributed to a reduction in G1-phase durations for all populations within the population of actively cycling cells with the exception of pre-selection DP thymocytes, whereas the S-phase duration was modestly increased in DN2, DN3b, and DN4 thymocytes and remained unaltered in DN3a and pre-selection DP cells (Figure 6G). We observed a substantial reduction in the fraction of long-G1 non-cycling cells in pre-selection DP thymocytes, thus reconciling experimental data of an increased fraction of cycling cells in pre-selection DP cells without the requirement for increased cell cycle speeds (Figure 6I). We conclude that thymic regeneration post-sublethal irradiation at cell cycle phase resolution is predominantly driven by increased rates of entry into the cycle and shortening of the G1 phase, but not the S phase, predominantly in thymocyte subsets characterized by slow turnover at steady state.

Thus, our studies reveal fundamental differences in how thymocytes adopt developmental-stage-dependent modulation of cell cycle length during steady-state T cell development and perturbation-induced adaptation of cell cycle speed within populations during the regenerative process.

DISCUSSION

Studies on T cell developmental dynamics in the thymus over the past decades have provided information on residence times, proliferation rates, and death during phases of selection within individual thymocyte populations[12,13,15] (for a review, see Krueger et al.[17]). However, their temporal resolution is insufficient to determine the duration of individual cell cycle phases. Such information is crucial to better understand the regulatory principles of proliferation dynamics at steady state and during therapy-induced regeneration.

Implications for thymocyte biology and regeneration

We accurately determined cell cycle phase durations in thymocytes of many distinct developmental stages at steady state. The transition between slowly and rapidly cycling thymocyte populations was characterized by the simultaneous contraction or expansion of G1 and S phases, supporting a so-called stretch model of cell cycle regulation. This type of cycling behavior was first described to explain the acceleration of B and T cell proliferation upon activation.[27] Similar to the situation of lymphocyte activation, thymocytes rapidly expand following β-selection from 4×10^5 to 10^8 cells, corresponding to 7 divisions within a period of only 2–4 days.[15,17] Contraction of both the G1 and S phases might constitute the optimal solution to accommodate faithful DNA replication along with a minimal G1 phase, similar to the cell cycle patterns observed in embryonic stem cells.[28] In line with a previous study, the G2/M-phase duration was uncoupled from stretching and contraction, and its short duration of less than 1.5 h indicated that thymocytes lack a sizable G2 phase.[29] The mechanisms controlling S-phase duration remain elusive. S-phase duration has been proposed to be determined by the number of active replication origins and to be driven by the activity of the E2F transcription factor family.[30,31] Recently, it has been reported that DNA replication speed was, in part, controlled by engaging dormant replication origins and/or the differential activity of replication stress checkpoints *in vivo*.[32]

Despite substantial numbers of cells in cell cycle pause, especially in populations rearranging TCR loci (DN3a and pre-selection DP), FUCCI G1 reporter protein levels suggested that these cells did not adopt a state of quiescence (G0). In line with an earlier study, a FUCCI-based quiescent state first emerged in DP thymocytes following selection, with quiescent cells accumulating in single-positive populations.[19,33] Although quiescence remains incompletely defined molecularly, a reduction in the expression of licensing factors, such as Cdc6 and Mcm2, and an increase in $p27^{kip1}$ in DP thymocytes support

Figure 5. Decision to re-enter the S phase after one round of cycling defines cell cycle heterogeneity

(A) Schematic representation of experiments. FUCCI DN3a thymocytes were sorted based on the presented gating strategy as $G1^{early}$ (gray, mAG^-mKO2^-), $G1^{int}$ (purple, mAG^-mKO2^+), and S (green, mAG^+mKO2^-). Target populations were co-cultured on OP9-DL1 feeder cells for up to 24 h, and FUCCI cell cycle profiles were assessed by flow cytometry every 2 h.

(B) Representative dot plots of $G1^{early}$, $G1^{int}$, and S DN3a thymocytes at indicated time points.

(C–E) Frequencies of the indicated target populations and their corresponding FUCCI profiles over time with (C) $G1^{early}$ (gray, mAG^-mKO2^-), (D) $G1^{int}$ (purple, mAG^-mKO2^+), and (E) S (green, mAG^+mKO2^-). Pooled data are from two independent experiments. Data are represented as mean ± SEM.

(F) DNA incorporation in cells re-entering S phase. The distribution of DNA is shown at logarithmic scale and rescaled between 2N and 4N using 2 h as reference for 2N. The percentage of cells and average DNA levels of cells separated based on their labeling by a mixture of two Gaussians for the displayed populations are shown (n = 1–3).

CellPress
OPEN ACCESS

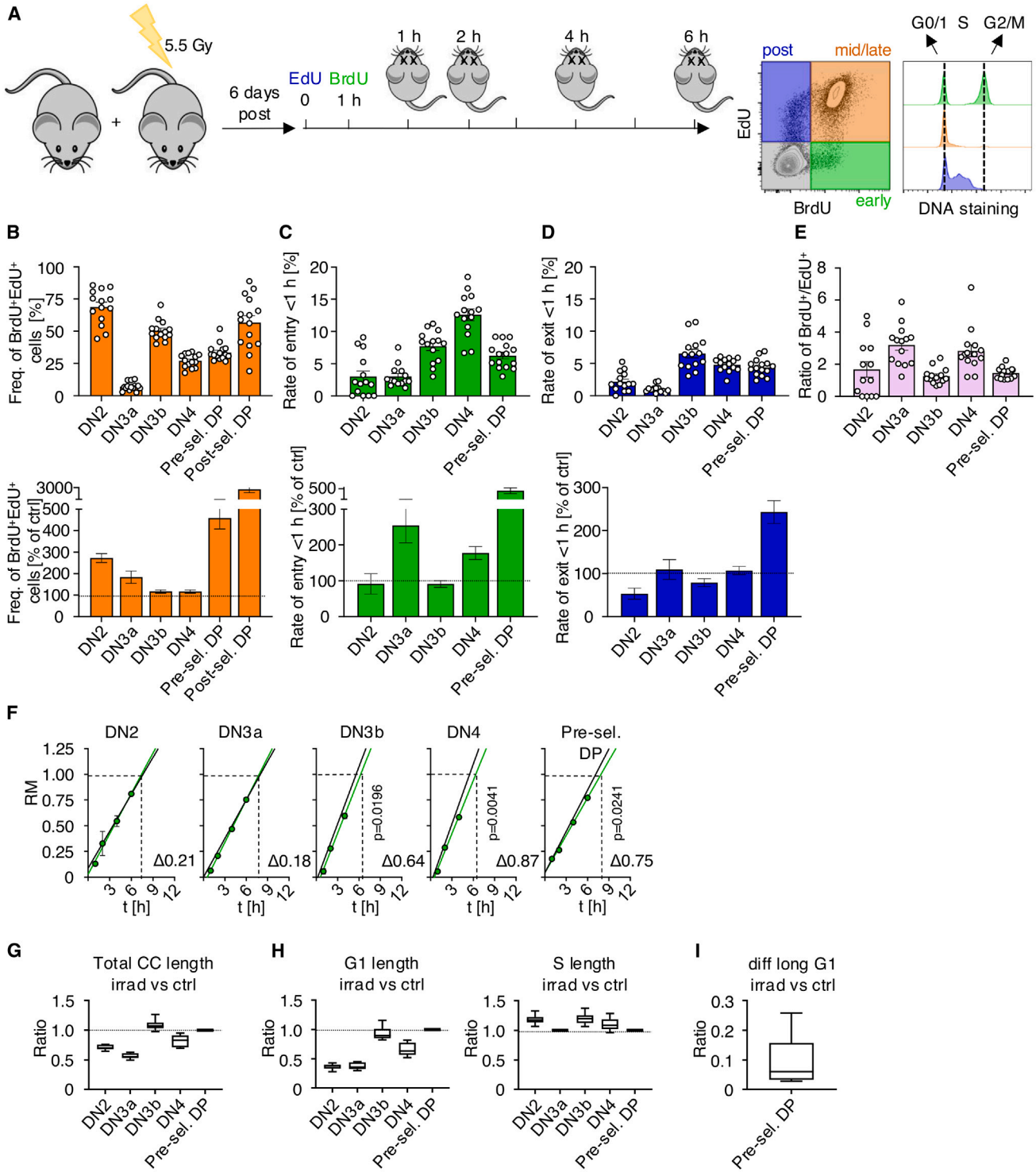

Figure 6. Population-specific cell cycle phase alterations determine thymus regeneration

(A) Schematic model of experiments.

(B–D) Top: frequencies of EdU^+BrdU^+ cells (B), EdU^-BrdU^+ cells (C), and EdU^+BrdU^- cells (D). Bottom: data are presented as the percentage of control (ctrl), with $n = 16$ ctrl mice and $n = 14–15$ irradiated mice. Data are represented as mean ± SEM. If data is presented as % of control, error bars indicate mean with SE.

(E) Ratio of $BrdU^+/EdU^+$ cells of thymocyte subpopulations of irradiated mice. Data are represented as mean ± SEM. $n = 14–15$ mice.

(F) Analysis of S-phase duration based on RM values of $BrdU^+$ cells (early S phase) of irradiated samples over time (green dots). Green line: linear regression. Black line: non-irradiated ctrl. Numbers adjacent to linear regression show the difference in S-phase time in h between ctrl and irradiated mice, with $n = 4$ ctrl mice

(legend continued on next page)

our conclusion.[34] Re-entry into the cell cycle requires longer intervals than passing through a prolonged G1 phase. We suggest that a prolonged G1 duration is more compatible with a developmentally programmed trajectory, whereas quiescence is likely to be more compatible with naive cells lying in wait for cognate antigens for undefined periods of time.

We noted distinct patterns of cell cycle heterogeneity. Heterogeneity in DN3b cells was best explained by varying G1-phase durations. In contrast, DN3a and pre-selection DP cell cycles were best explained by including a subpopulation with a prolonged G1 phase that is not actively cycling. It is plausible that these subpopulations comprise cells undergoing TCR gene rearrangements, whereas actively cycling populations may comprise cells transitioning into or out of the respective subsets. In fact, a recent single-cell RNA sequencing (scRNA-seq) study has demonstrated that upon entry into the DP stage, thymocytes complete exactly one round of division before cycling ceases.[35] Cell cycle heterogeneity was also apparent during longitudinal follow-up of cells and upon *in vitro* differentiation, substantiating the predictions derived from the ABM that variation is largely situated in the G1 phase, whereas the transition from S to G1 is kinetically fixed, in accordance with the virtually constant durations of the G2 and M phases. Our experimental setup permits the tracking of little more than one full cell cycle. Thus, it remains open whether the observed heterogeneity is based on functional differences even in phenotypically identical populations or due to unequal access to growth factors, such as interleukin (IL)-7 or exposure to pre-TCR ligands, which were recently proposed as contributors to β-selection.[36,37] Cells may also display intrinsic stochasticity, which has been proposed as a factor in developmental processes, such as hematopoietic lineage decisions.[38,39] Finally, it is possible that a cell's decision to divide is predetermined by its ancestry or determined by size boundaries or nutrient availability.[40] Evidence for such a scenario is provided by studies of *in vitro* activation of B and T cells, upon which daughters of the same parent cells display similar division destinies.[2,41,42]

To our surprise, thymocytes did not further increase cell cycle speed following a stretch model during thymus regeneration. Rather, we observed substantially shorter G1 phases and the recruitment of cells from the non-cycling pool, whereas S phases remained constant or were even slightly extended. These findings are consistent with the possibility that feedback mechanisms controlling regeneration depend on extrinsic signals, to which cells preferentially respond during the G1 phase. Thymic regeneration is governed by a complex interplay of dying thymocytes and endothelial and epithelial cells interacting via IL-23 and BMP4, ultimately resulting in increased expression of the Notch ligand DLL4 on epithelial cells. Hence, in the process of regeneration, thymocytes are likely to encounter a higher density of growth-supporting ligands.[43,44] In contrast, the S-phase duration was developmentally preprogrammed at the population level but not critically affected upon perturbation. Furthermore, the activation of DNA damage checkpoints following irradiation may also counteract further contraction of S phases.[32,45] Our analysis is focused on an individual time point, representing the partial recovery of all populations. As thymocyte populations display unequal recovery rates, our analysis might rather underestimate cell cycle phase alterations during regeneration.[24] In the absence of perturbation, thymocyte numbers start to decline in mice from 6 weeks of age, with the emergence of age-associated epithelial cells, which may impact cell cycle behavior and could be further studied with our approach.[46–48]

To date, it remains elusive whether developmental transitions occur at defined cell cycle phases. Resolving this question is complicated by the fact that marker-defined population boundaries as defined in the paradigmatic DN-DP-SP thymocyte scheme do not necessarily reflect transitions in the biological state. For instance, T lineage commitment occurs at some point in DN2 (the DN2a > DN2b transition).[9–11] The onset of somatic recombination can occur in DN2b at an interval from commitment that remains to be defined or in DN3a.[49] Similarly, there is no obvious biological difference between DN3b and DN4 apart from proliferation age, and this population might, by 1 division, even expand to early DP cells.[35]

Mathematical modeling of cell cycle dynamics

Mathematical modeling has been previously used to extract complex quantitative properties of T cell development.[16,50] We have used an ABM approach, allowing us to control the heterogeneity of phase durations.[22] Alternative approaches include ordinary differential equations (ODEs), which simulate the number of cells in each phase over time.[16] While ODEs can sometimes provide analytical formulas for pulse labeling, they structurally impose an exponentially distributed duration for each phase, allowing some cells to cycle implausibly fast.[51] This makes it difficult to compare synchronous or heterogeneous phase durations. Additionally, ODE models often predict extremely short or long cell cycles, which can be challenging to reconcile with experimental data.[52,53] A recent ODE-based study separated the cell cycle of DP thymocytes into multiple progression steps, with a final step of quiescent cells.[54] That study extracted a similar cell cycle duration, although a direct comparison is limited due to the pooling of pre- and post-selection DPs in their study. Alternatively, age- or DNA-structured models that account for a distribution of age or DNA inside each cell phase could constitute a valuable alternative since they include heterogeneity and, unlike ODEs, can introduce a minimum residence time in each cell cycle phase.[55–57] Cyton2, a recent development accounting for inheritance or correlations between daughter cells at division, could be integrated with novel experimental techniques to further refine our understanding of T cell development.[22,58]

and n = 1–4 irradiated WT mice for each time point. An analysis of significance between ctrl and irradiated mice was performed using an unpaired t test for the latest time point.

(G) Total cell cycle length ratio of irradiated vs. ctrl thymocyte subsets.

(H) G1- (left) or S-phase length (right) ratio of irradiated vs. ctrl thymocyte subsets (n = 1–10).

(I) Difference of long-G1 cells indicated by the ratio of irradiated vs. ctrl pre-selection DP thymocytes (n = 9). (G–I) Error bars display the SD of 10 independent fits.

Conclusion

Taken together, the results of our study provide a combined experimental and computational framework to accurately determine cell cycle phase durations *in vivo*, integrating intra-population heterogeneity. We propose that this combination is widely applicable across organ systems and disease conditions. In the case of intrathymic T cell development at steady state and during regeneration, our study has revealed a broad and population-specific spectrum of cell cycle adaptation to proliferative requirements. These findings illustrate the need for refined cell cycle analysis in situations of loss of proliferation control, such as cancer, or regenerative processes.

Limitations of this study

It still remains a challenge to simulate T cell development in all its complexity in an all-encompassing model. In the ABM, we have used a pool of bystander cells in long G1. The longer the time window, the more continuous properties may add discrepancies between model simulations and experimental data, such as a continuous distribution of extremely long G1 durations or the entry of new labeled cells into the long G1 pool. During regeneration, thymocyte populations are still subject to dynamical changes. Similarly, thymocyte numbers in non-manipulated mice are subject to constant changes, with numbers increasing until 4–6 weeks of age, followed by age-related thymus involution.[46] Although, technically, non-steady-state conditions apply, and this might influence the dynamics of labeling at the timescale of one cell cycle, the population sizes remain essentially constant and can be considered as *bona fide* steady state for the purpose of this analysis. Further adaptations to account for non-equilibrium effects in rapidly growing populations would be particularly interesting for the field of cancer biology.

RESOURCE AVAILABILITY

Lead contact

Further information and requests for resources and reagents should be directed to and will be fulfilled by the lead contact, Andreas Krueger (Andreas.Krueger@immu.bio.uni-giessen.de).

Materials availability

This study did not generate new unique reagents.

Data and code availability

- The code for the mathematical model is available at Zenodo (https://zenodo.org/records/14169223),[59] provided together with the Moonfit package.[60]
- The raw data used for simulations is provided at Zenodo: https://zenodo.org/records/14169223.
- Any additional information required to re-analyze the data reported in this paper is available from the lead contact upon request.

ACKNOWLEDGMENTS

We are grateful to Dr. Jonas Blume and Eleni Dapergola for technical help during the early phase of the project. We are grateful to Julia Häusler and Bedriska Reitz for technical support. We thank Prof. Dr. Anja Hauser (DRFZ Berlin) for providing the FUCCI mouse line and Dr. Ines Kühnel for a critical reading of the manuscript and helpful discussions. This work was funded by grants from the German Research Foundation (DFG) (KR2320/6-1 and EXC62 "REBIRTH") to A.K.

AUTHOR CONTRIBUTIONS

H.K.-S., P.A.R., M.M.-H., and A.K. designed all experiments and analyzed data. H.K.-S. and Z.G. conducted all experiments. P.A.R. generated the mathematical model and performed simulations. N.A.V. analyzed data. H.K.-S., P.A.R., V.G., M.M.-H., and A.K. wrote the manuscript.

DECLARATION OF INTERESTS

The authors declare no competing interests.

STAR★METHODS

Detailed methods are provided in the online version of this paper and include the following:

- KEY RESOURCES TABLE
- EXPERIMENTAL MODEL AND STUDY PARTICIPANT DETAILS
  - *In vivo* animal studies
- METHOD DETAILS
  - Flow cytometry
  - Cell preparations
  - Dual pulse labeling using EdU and BrdU
  - Thymus regeneration
- QUANTIFICATION AND STATISTICAL ANALYSIS
  - Agent-based model

SUPPLEMENTAL INFORMATION

Supplemental information can be found online at https://doi.org/10.1016/j.celrep.2024.115132.

Received: August 23, 2024
Revised: October 14, 2024
Accepted: December 11, 2024
Published: January 3, 2025

REFERENCES

1. Gitlin, A.D., Mayer, C.T., Oliveira, T.Y., Shulman, Z., Jones, M.J.K., Koren, A., and Nussenzweig, M.C. (2015). T cell help controls the speed of the cell cycle in germinal center B cells. Science *349*, 643–646.
2. Heinzel, S., Binh Giang, T., Kan, A., Marchingo, J.M., Lye, B.K., Corcoran, L.M., and Hodgkin, P.D. (2017). A Myc-dependent division timer complements a cell-death timer to regulate T cell and B cell responses. Nat. Immunol. *18*, 96–103. https://doi.org/10.1038/ni.3598.
3. Zotos, D., Quast, I., Li-Wai-Suen, C.S.N., McKenzie, C.I., Robinson, M.J., Kan, A., Smyth, G.K., Hodgkin, P.D., and Tarlinton, D.M. (2021). The concerted change in the distribution of cell cycle phases and zone composition in germinal centers is regulated by IL-21. Nat. Commun. *12*, 7160. https://doi.org/10.1038/s41467-021-27477-0.
4. Ziętara, N., Łyszkiewicz, M., Puchałka, J., Witzlau, K., Reinhardt, A., Förster, R., Pabst, O., Prinz, I., and Krueger, A. (2015). Multicongenic fate mapping quantification of dynamics of thymus colonization. J. Exp. Med. *212*, 1589–1601.
5. Zlotoff, D.A., Sambandam, A., Logan, T.D., Bell, J.J., Schwarz, B.A., and Bhandoola, A. (2010). CCR7 and CCR9 together recruit hematopoietic progenitors to the adult thymus. Blood *115*, 1897–1905. https://doi.org/10.1182/blood-2009-08-237784.
6. Krueger, A., Willenzon, S., Łyszkiewicz, M., Kremmer, E., and Förster, R. (2010). CC chemokine receptor 7 and 9 double-deficient hematopoietic progenitors are severely impaired in seeding the adult thymus. Blood *115*, 1906–1912.
7. Allman, D., Sambandam, A., Kim, S., Miller, J.P., Pagan, A., Well, D., Meraz, A., and Bhandoola, A. (2003). Thymopoiesis independent of

common lymphoid progenitors. Nat. Immunol. *4*, 168–174. https://doi.org/10.1038/ni878.

8. Schwarz, B.A., and Bhandoola, A. (2004). Circulating hematopoietic progenitors with T lineage potential. Nat. Immunol. *5*, 953–960.
9. Ikawa, T., Hirose, S., Masuda, K., Kakugawa, K., Satoh, R., Shibano-Satoh, A., Kominami, R., Katsura, Y., and Kawamoto, H. (2010). An essential developmental checkpoint for production of the T cell lineage. Science *329*, 93–96. https://doi.org/10.1126/science.1188995.
10. Li, P., Burke, S., Wang, J., Chen, X., Ortiz, M., Lee, S.C., Lu, D., Campos, L., Goulding, D., Ng, B.L., et al. (2010). Reprogramming of T cells to natural killer-like cells upon Bcl11b deletion. Science *329*, 85–89. https://doi.org/10.1126/science.1188063.
11. Li, L., Leid, M., and Rothenberg, E.V. (2010). An early T cell lineage commitment checkpoint dependent on the transcription factor Bcl11b. Science *329*, 89–93. https://doi.org/10.1126/science.1188989.
12. Egerton, M., and Scollay, R. (1990). Intrathymic selection of murine TCR alpha beta+CD4-CD8- thymocytes. Int. Immunol. *2*, 157–163. https://doi.org/10.1093/intimm/2.2.157.
13. Porritt, H.E., Gordon, K., and Petrie, H.T. (2003). Kinetics of Steady-state Differentiation and Mapping of Intrathymic-signaling Environments by Stem Cell Transplantation in Nonirradiated Mice. J. Exp. Med. *198*, 957–962.
14. Shortman, K., Vremec, D., and Egerton, M. (1991). The kinetics of T cell antigen receptor expression by subgroups of CD4+8+ thymocytes: delineation of CD4+8+3(2+) thymocytes as post-selection intermediates leading to mature T cells. J. Exp. Med. *173*, 323–332. https://doi.org/10.1084/jem.173.2.323.
15. Pénit, C., Lucas, B., and Vasseur, F. (1995). Cell expansion and growth arrest phases during the transition from precursor (CD4-8-) to immature (CD4+8+) thymocytes in normal and genetically modified mice. J. Immunol. *154*, 5103.
16. Robert, P.A., Kunze-Schumacher, H., Greiff, V., and Krueger, A. (2021). Modeling the Dynamics of T-Cell Development in the Thymus. Entropy *23*, 437. https://doi.org/10.3390/e23040437.
17. Krueger, A., Ziętara, N., and Łyszkiewicz, M. (2017). T Cell Development by the Numbers. Trends Immunol. *38*, 128–139. https://doi.org/10.1016/j.it.2016.10.007.
18. Surh, C.D., and Sprent, J. (1994). T-cell apoptosis detected in situ during positive and negative selection in the thymus. Nature *372*, 100–103. https://doi.org/10.1038/372100a0.
19. Tomura, M., Sakaue-Sawano, A., Mori, Y., Takase-Utsugi, M., Hata, A., Ohtawa, K., Kanagawa, O., and Miyawaki, A. (2013). Contrasting quiescent G0 phase with mitotic cell cycling in the mouse immune system. PLoS One *8*, e73801. https://doi.org/10.1371/journal.pone.0073801.
20. Maltsev, D.I., Mellanson, K.A., Belousov, V.V., Enikolopov, G.N., and Podgorny, O.V. (2022). The bioavailability time of commonly used thymidine analogues after intraperitoneal delivery in mice: labeling kinetics in vivo and clearance from blood serum. Histochem. Cell Biol. *157*, 239–250. https://doi.org/10.1007/s00418-021-02048-y.
21. Begg, A.C., McNally, N.J., Shrieve, D.C., and Kärcher, H. (1985). A method to measure the duration of DNA synthesis and the potential doubling time from a single sample. Cytometry *6*, 620–626. https://doi.org/10.1002/cyto.990060618.
22. Hawkins, E.D., Turner, M.L., Dowling, M.R., van Gend, C., and Hodgkin, P.D. (2007). A model of immune regulation as a consequence of randomized lymphocyte division and death times. Proc. Natl. Acad. Sci. USA *104*, 5032–5037. https://doi.org/10.1073/pnas.0700026104.
23. Awong, G., LaMotte-Mohs, R., and Zúñiga-Pflücker, J.C. (2010). Key players for T-cell regeneration. Curr. Opin. Hematol. *17*, 327–332. https://doi.org/10.1097/MOH.0b013e3283395133.
24. Kaneko, K.B., Tateishi, R., Miyao, T., Takakura, Y., Akiyama, N., Yokota, R., Akiyama, T., and Kobayashi, T.J. (2019). Quantitative analysis reveals reciprocal regulations underlying recovery dynamics of thymocytes and thymic environment in mice. Commun. Biol. *2*, 444. https://doi.org/10.1038/s42003-019-0688-8.
25. Kunze-Schumacher, H., Winter, S.J., Imelmann, E., and Krueger, A. (2018). miRNA miR-21 Is Largely Dispensable for Intrathymic T-Cell Development. Front. Immunol. *9*, 2497. https://doi.org/10.3389/fimmu.2018.02497.
26. Dudakov, J.A., Hanash, A.M., Jenq, R.R., Young, L.F., Ghosh, A., Singer, N.V., West, M.L., Smith, O.M., Holland, A.M., Tsai, J.J., et al. (2012). Interleukin-22 drives endogenous thymic regeneration in mice. Science *336*, 91–95. https://doi.org/10.1126/science.1218004.
27. Dowling, M.R., Kan, A., Heinzel, S., Zhou, J.H.S., Marchingo, J.M., Wellard, C.J., Markham, J.F., and Hodgkin, P.D. (2014). Stretched cell cycle model for proliferating lymphocytes. Proc. Natl. Acad. Sci. USA *111*, 6377–6382. https://doi.org/10.1073/pnas.1322420111.
28. Becker, K.A., Ghule, P.N., Therrien, J.A., Lian, J.B., Stein, J.L., van Wijnen, A.J., and Stein, G.S. (2006). Self-renewal of human embryonic stem cells is supported by a shortened G1 cell cycle phase. J. Cell. Physiol. *209*, 883–893. https://doi.org/10.1002/jcp.20776.
29. Araujo, A.R., Gelens, L., Sheriff, R.S.M., and Santos, S.D.M. (2016). Positive Feedback Keeps Duration of Mitosis Temporally Insulated from Upstream Cell-Cycle Events. Mol. Cell *64*, 362–375. https://doi.org/10.1016/j.molcel.2016.09.018.
30. Greenberg, A., and Simon, I. (2022). S Phase Duration Is Determined by Local Rate and Global Organization of Replication. Biology *11*, 718. https://doi.org/10.3390/biology11050718.
31. Pennycook, B.R., Vesela, E., Peripolli, S., Singh, T., Barr, A.R., Bertoli, C., and de Bruin, R.A.M. (2020). E2F-dependent transcription determines replication capacity and S phase length. Nat. Commun. *11*, 3503. https://doi.org/10.1038/s41467-020-17146-z.
32. Rossetti, G.G., Dommann, N., Karamichali, A., Dionellis, V.S., Asensio Aldave, A., Yarahmadov, T., Rodriguez-Carballo, E., Keogh, A., Candinas, D., Stroka, D., and Halazonetis, T.D. (2024). In vivo DNA replication dynamics unveil aging-dependent replication stress. Cell *187*, 6220–6234.e13. https://doi.org/10.1016/j.cell.2024.08.034.
33. Föhse, L., Reinhardt, A., Oberdörfer, L., Schmitz, S., Förster, R., Malissen, B., and Prinz, I. (2013). Differential postselection proliferation dynamics of αβ T cells, Foxp3+ regulatory T cells, and invariant NKT cells monitored by genetic pulse labeling. J. Immunol. *191*, 2384–2392. https://doi.org/10.4049/jimmunol.1301359.
34. Narayan, K., Sylvia, K.E., Malhotra, N., Yin, C.C., Martens, G., Vallerskog, T., Kornfeld, H., Xiong, N., Cohen, N.R., Brenner, M.B., et al. (2012). Intrathymic programming of effector fates in three molecularly distinct γδ T cell subtypes. Nat. Immunol. *13*, 511–518. https://doi.org/10.1038/ni.2247.
35. Li, Y., Li, K., Zhu, L., Li, B., Zong, D., Cai, P., Jiang, C., Du, P., Lin, J., and Qu, K. (2021). Development of double-positive thymocytes at single-cell resolution. Genome Med. *13*, 49.
36. Boudil, A., Matei, I.R., Shih, H.Y., Bogdanoski, G., Yuan, J.S., Chang, S.G., Montpellier, B., Kowalski, P.E., Voisin, V., Bashir, S., et al. (2015). IL-7 coordinates proliferation, differentiation and Tcra recombination during thymocyte β-selection. Nat. Immunol. *16*, 397–405. https://doi.org/10.1038/ni.3122.
37. Duke-Cohan, J.S., Akitsu, A., Mallis, R.J., Messier, C.M., Lizotte, P.H., Aster, J.C., Hwang, W., Lang, M.J., and Reinherz, E.L. (2023). Pre-T cell receptor self-MHC sampling restricts thymocyte dedifferentiation. Nature *613*, 565–574. https://doi.org/10.1038/s41586-022-05555-7.
38. Rué, P., and Martinez Arias, A. (2015). Cell dynamics and gene expression control in tissue homeostasis and development. Mol. Syst. Biol. *11*, 792. https://doi.org/10.15252/msb.20145549.
39. Chang, H.H., Hemberg, M., Barahona, M., Ingber, D.E., and Huang, S. (2008). Transcriptome-wide noise controls lineage choice in mammalian progenitor cells. Nature *453*, 544–547. https://doi.org/10.1038/nature06965.

40. Andersson, E., Rothenberg, E.V., Peterson, C., and Olariu, V. (2024). T-cell commitment inheritance-an agent-based multi-scale model. NPJ Syst. Biol. Appl. *10*, 40. https://doi.org/10.1038/s41540-024-00368-y.

41. Hawkins, E.D., Markham, J.F., McGuinness, L.P., and Hodgkin, P.D. (2009). A single-cell pedigree analysis of alternative stochastic lymphocyte fates. Proc. Natl. Acad. Sci. USA *106*, 13457–13462. https://doi.org/10.1073/pnas.0905629106.

42. Duffy, K.R., Wellard, C.J., Markham, J.F., Zhou, J.H.S., Holmberg, R., Hawkins, E.D., Hasbold, J., Dowling, M.R., and Hodgkin, P.D. (2012). Activation-induced B cell fates are selected by intracellular stochastic competition. Science *335*, 338–341. https://doi.org/10.1126/science.1213230.

43. Wertheimer, T., Velardi, E., Tsai, J., Cooper, K., Xiao, S., Kloss, C.C., Ottmüller, K.J., Mokhtari, Z., Brede, C., deRoos, P., et al. (2018). Production of BMP4 by endothelial cells is crucial for endogenous thymic regeneration. Sci. Immunol. *3*, eaal2736. https://doi.org/10.1126/sciimmunol.aal2736.

44. Kinsella, S., Evandy, C.A., Cooper, K., Iovino, L., deRoos, P.C., Hopwo, K.S., Granadier, D.W., Smith, C.W., Rafii, S., and Dudakov, J.A. (2021). Attenuation of apoptotic cell detection triggers thymic regeneration after damage. Cell Rep. *37*, 109789. https://doi.org/10.1016/j.celrep.2021.109789.

45. Calvo-Asensio, I., Sugrue, T., Bosco, N., Rolink, A., and Ceredig, R. (2018). DN2 Thymocytes Activate a Specific Robust DNA Damage Response to Ionizing Radiation-Induced DNA Double-Strand Breaks. Front. Immunol. *9*, 1312. https://doi.org/10.3389/fimmu.2018.01312.

46. Palmer, S., Albergante, L., Blackburn, C.C., and Newman, T.J. (2018). Thymic involution and rising disease incidence with age. Proc. Natl. Acad. Sci. USA *115*, 1883–1888. https://doi.org/10.1073/pnas.1714478115.

47. Cowan, J.E., Takahama, Y., Bhandoola, A., and Ohigashi, I. (2020). Postnatal Involution and Counter-Involution of the Thymus. Front. Immunol. *11*, 897. https://doi.org/10.3389/fimmu.2020.00897.

48. Kousa, A.I., Jahn, L., Zhao, K., Flores, A.E., Acenas, D., Lederer, E., Argyropoulos, K.V., Lemarquis, A.L., Granadier, D., Cooper, K., et al. (2024). Age-related epithelial defects limit thymic function and regeneration. Nat. Immunol. *25*, 1593–1606. https://doi.org/10.1038/s41590-024-01915-9.

49. Livák, F., Tourigny, M., Schatz, D.G., and Petrie, H.T. (1999). Characterization of TCR gene rearrangements during adult murine T cell development. J. Immunol. *162*, 2575–2580.

50. Yates, A.J. (2014). Theories and Quantification of Thymic Selection. Front. Immunol. *5*, 13. https://doi.org/10.3389/fimmu.2014.00013.

51. Simms, K., Bean, N., and Koerber, A. (2012). A mathematical model of cell cycle progression applied to the MCF-7 breast cancer cell line. Bull. Math. Biol. *74*, 736–767. https://doi.org/10.1007/s11538-011-9700-2.

52. Vibert, J., and Thomas-Vaslin, V. (2017). Modelling T cell proliferation: Dynamics heterogeneity depending on cell differentiation, age, and genetic background. PLoS Comput. Biol. *13*, e1005417. https://doi.org/10.1371/journal.pcbi.1005417.

53. Ramos, C.V., Ballesteros-Arias, L., Silva, J.G., Paiva, R.A., Nogueira, M.F., Carneiro, J., Gjini, E., and Martins, V.C. (2020). Cell Competition, the Kinetics of Thymopoiesis, and Thymus Cellularity Are Regulated by Double-Negative 2 to 3 Early Thymocytes. Cell Rep. *32*, 107910. https://doi.org/10.1016/j.celrep.2020.107910.

54. Jolly, A., Fanti, A.K., Kongsaysak-Lengyel, C., Claudino, N., Gräßer, I., Becker, N.B., and Höfer, T. (2022). CycleFlow simultaneously quantifies cell-cycle phase lengths and quiescence in vivo. Cell Rep. Methods *2*, 100315. https://doi.org/10.1016/j.crmeth.2022.100315.

55. Zilman, A., Ganusov, V.V., and Perelson, A.S. (2010). Stochastic Models of Lymphocyte Proliferation and Death. PLoS One *5*, e12775.

56. Basse, B., Baguley, B.C., Marshall, E.S., Joseph, W.R., van Brunt, B., Wake, G., and Wall, D.J.N. (2003). A mathematical model for analysis of the cell cycle in cell lines derived from human tumors. J. Math. Biol. *47*, 295–312. https://doi.org/10.1007/s00285-003-0203-0.

57. Celora, G.L., Bader, S.B., Hammond, E.M., Maini, P.K., Pitt-Francis, J.M., and Byrne, H.M. (2022). A DNA-structured mathematical model of cell-cycle progression in cyclic hypoxia. J. Theor. Biol. *545*, 111104. https://doi.org/10.1016/j.jtbi.2022.111104.

58. Cheon, H., Kan, A., Prevedello, G., Oostindie, S.C., Dovedi, S.J., Hawkins, E.D., Marchingo, J.M., Heinzel, S., Duffy, K.R., and Hodgkin, P.D. (2021). Cyton2: A Model of Immune Cell Population Dynamics That Includes Familial Instructional Inheritance. Front. Bioinform. *1*, 723337. https://doi.org/10.3389/fbinf.2021.723337.

59. High Resolution Simulation of Thymocyte Cell Cycling https://doi.org/10.5281/zenodo.14169223.

60. Robert, P.A., Jönsson, H., and Meyer-Hermann, M. (2018). MoonFit, a minimal interface for fitting ODE dynamical models, bridging simulation by experimentalists and customization by C++ programmers. Preprint at bioRxiv. https://doi.org/10.1101/281188.

61. Weber, T.S., Jaehnert, I., Schichor, C., Or-Guil, M., and Carneiro, J. (2014). Quantifying the length and variance of the eukaryotic cell cycle phases by a stochastic model and dual nucleoside pulse labelling. PLoS Comput. Biol. *10*, e1003616. https://doi.org/10.1371/journal.pcbi.1003616.

62. Manesso, E., Chickarmane, V., Kueh, H.Y., Rothenberg, E.V., and Peterson, C. (2013). Computational modelling of T-cell formation kinetics: output regulated by initial proliferation-linked deferral of developmental competence. J. R. Soc. Interface *10*, 20120774. https://doi.org/10.1098/rsif.2012.0774.

63. Thomas-Vaslin, V., Altes, H.K., de Boer, R.J., and Klatzmann, D. (2008). Comprehensive assessment and mathematical modeling of T cell population dynamics and homeostasis. J. Immunol. *180*, 2240–2250. https://doi.org/10.4049/jimmunol.180.4.2240.

64. Elfaki, Y., Robert, P.A., Binz, C., Falk, C.S., Bruder, D., Prinz, I., Floess, S., Meyer-Hermann, M., and Huehn, J. (2021). Influenza A virus-induced thymus atrophy differentially affects dynamics of conventional and regulatory T-cell development in mice. Eur. J. Immunol. *51*, 1166–1181. https://doi.org/10.1002/eji.202048981.

65. Hagan, M.P. (1984). Cell proliferation kinetics analyzed with BrdU and near-UV light treatment. Bibl. Haematol. *48*, 384–401. https://doi.org/10.1159/000408411.

66. Matiašová, A., Sevc, J., Mikeš, J., Jendželovský, R., Daxnerová, Z., and Fedoročko, P. (2014). Flow cytometric determination of 5-bromo-2'-deoxyuridine pharmacokinetics in blood serum after intraperitoneal administration to rats and mice. Histochem. Cell Biol. *142*, 703–712. https://doi.org/10.1007/s00418-014-1253-7.

STAR★METHODS

KEY RESOURCES TABLE

REAGENT or RESOURCE	SOURCE	IDENTIFIER
FACS antibodies (clone)		
Monoclonal anti-BrdU antibody (3D4), FITC	BioLegend	Cat#364104; RRID: AB_2564481
Monoclonal anti-mouse CD4 (GK1.5), PE-Cy7	BioLegend	Cat#100422; RRID: AB_312707
Monoclonal anti-mouse CD4 (GK1.5), PerCP-Cy5.5	BioLegend	Cat#100434; RRID: AB_893324
IgM anti-mouse CD4 (RL1.72)	Own production	Duke-Cohan[37]
Monoclonal anti-mouse CD8α (53–6.7), BV510	BioLegend	Cat#100751; RRID: AB_2561389
Monoclonal anti-mouse CD8α (53–6.7), PE-Cy7	BioLegend	Cat#100722; RRID: AB_312761
IgM anti-mouse CD8 (M31)	Own production	Rué and Martinez Arias[38]
Monoclonal anti-mouse CD25 (PC61), BV421	BioLegend	Cat#102034; RRID: AB_11203373
Monoclonal anti-mouse CD25 (PC61), PerCP-Cy5.5	BioLegend	Cat#102030; RRID: AB_893288
Monoclonal anti-mouse CD28 (E18), PE	BioLegend	Cat#122010; RRID: AB_604078
Monoclonal anti-mouse CD44 (IM7), APC-Cy7	BioLegend	Cat#103028; RRID: AB_830785
Monoclonal anti-mouse CD44 (IM7), PerCP-Cy5.5	BioLegend	Cat#103032; RRID: AB_2076204
Monoclonal anti-mouse CD69 (H1.2F3), PE	BioLegend	Cat#104508; RRID: AB_313111
Monoclonal anti-mouse CD69 (H1.2F3), APC	BioLegend	Cat#104514; RRID: AB_492843
Monoclonal anti-mouse CD71 (RI7217), APC	BioLegend	Cat#113819; RRID: AB_2728134
Monoclonal anti-mouse CD117 (2B8), APC-Cy7	BioLegend	Cat#105826; RRID: AB_1626278
Monoclonal anti-mouse TCRβ (H57-597), BV421	Biolegend	Cat#109230; RRID: AB_ 2562562
Monoclonal anti-mouse TCRβ (H57-597), APC-Cy7	BioLegend	Cat#109220; RRID: AB_893624
Monoclonal anti-mouse TCRβ (H57-597), PE-Cy7	BioLegend	Cat#109222; RRID: AB_ 893625
Chemicals		
DAPI (4′,6-Diamidino-2-Phenylindole, Dilactate)	BioLegend	Cat#422801
Bromodeoxyuridine (BrdU)	BioLegend	Cat#423401
DNase I from bovine pancreas	Sigma-Aldrich	Cat#D4513
EdU	Thermo Fisher Scientific	Cat#A10044
Low-Tox®-M Rabbit Complement	Cedarlane	Cat#CL3051
Lympholyte-M	Cedarlane	Cat#CL5031
Permeabilization Buffer Plus	BD Biosciences	Cat#561654
Critical commercial assays		
Click-iT™ Plus EdU Alexa Fluor™647 Flow Cytometry Assay Kit	Thermo Fisher Scientific	Cat#C10635

(*Continued on next page*)

Continued

REAGENT or RESOURCE	SOURCE	IDENTIFIER
Fixation/Permeabilization Solution Kit	BD Biosciences	Cat#554714
Experimental models: Organisms/strains		
Mouse: C57BL/6J (WT)	Janvier Labs/Charles River	N/A
Mouse: FUCCI (B6; Cg-Tg(FucciSG2M)$^{\#474Bsi}$-Tg(FucciG1)$^{\#639Bsi}$)	RIKEN	RBRC02704, RBRC02709
Software and algorithms		
GraphPad Prism 7	GraphPad Software	https://www.graphpad.com/ RRID: SCR_002798
FlowJo 10^{TM}	BD Biosciences	https://www.flowjo.com/solutions/flowjo RRID: SCR_008520
Code for the mathematical model	Zenodo	https://zenodo.org/records/14169223

EXPERIMENTAL MODEL AND STUDY PARTICIPANT DETAILS

In vivo animal studies

C57BL/6J (WT) mice were purchased from Janvier Labs or Charles River. FUCCI mice were bred at the ZFE, Goethe University Frankfurt and at the ZVTH, Justus-Liebig-University Giessen. For all experiments, male and female mice were used between 8 and 12 weeks of age. All animal experiments were performed in accordance with German law on care and use of laboratory animals (licenses: RP Darmstadt, FU1155; JLU Giessen, 818_M).

METHOD DETAILS

Flow cytometry

Monoclonal antibodies specific for CD4 (GK1.5), CD8α (53–6.7), CD25 (PC61.5), CD28 (E18), CD44 (IM7), CD69 (H1.2F3), CD71 (RI7217), CD117 (2B8) and TCRβ (H57-597) were used conjugated to Brilliant Violet (BV) 421, phycoerythrin (PE), peridinin chlorophyll protein-Cy5.5 (PerCP-Cy5.5), PE-Cy7, Allophycocyanin (APC) or APC-Cy7 and were purchased from BioLegend. Cells were acquired using a BD FACSCanto II (BD Biosciences) and data was processed using FlowJo software (BD Biosciences). For data analysis, doublets and cells in sub-G0/G1 phase were excluded. For all panels, cells were defined as ETPs ($CD117^{hi}CD25^{-}CD44^{+}$), DN1 ($CD25^{-}CD44^{+}$), DN2 ($CD25^{+}CD44^{+}$), DN2a ($CD117^{hi}CD25^{+}CD44^{+}$), DN2b ($CD117^{lo}CD25^{+}CD44^{+}$), DN3a ($CD25^{+}CD44^{-}CD28^{-}$ or $CD25^{+}CD44^{-}CD71^{-}$), DN3b ($CD25^{+}CD44^{-}CD28^{+}$ or $CD25^{+}CD44^{-}CD71^{+}$), DN4 $CD25^{-}CD44^{-}CD28^{+}$, pre-selection DP ($CD4^{+}CD8^{+}CD69^{-}TCR\beta^{-}$), post-selection DP ($CD4^{+}CD8^{+}CD69^{+}TCR\beta^{+}$), SP4 ($TCR\beta^{+}$, $CD4^{+}$) and SP8 ($TCR\beta^{+}$, $CD8^{+}$).

Cell preparations

Thymi were meshed through a 70 μm cell strainer (Corning) to obtain single-cell suspensions. Cell numbers were determined using a CASY Cell Counter and Analyzer Model TT (Innovatis).

Dual pulse labeling using EdU and BrdU

For analysis of nucleoside analogue incorporation, mice were first intravenously injected with 1 mg EdU (Thermo Fisher Scientific) followed by 2 mg BrdU (BioLegend) 60 min later. Then, thymi were harvested at indicated time points. Single-cell suspensions were stained with monoclonal antibodies followed by EdU and BrdU staining procedures according to the manufacturer's instructions using the Click-iT Plus EdU Alexa Fluor 647 Flow Cytometry Assay Kit (Thermo Fisher Scientific), BD Cytofix/Cytoperm (BD Biosciences), Permeabilization Buffer Plus (BD Biosciences) and treatment with DNase I from bovine pancreas (Sigma-Aldrich). To detect BrdU, samples were subsequently stained with FITC-conjugated anti-BrdU antibody (3D4, BioLegend). DNA content was analyzed by staining cells with DAPI (BioLegend).

Thymus regeneration

WT mice were sublethally irradiated (5.5 Gy). 6 days post irradiation, EdU/BrdU dual pulse labeling was performed as described before.

QUANTIFICATION AND STATISTICAL ANALYSIS

All statistical analysis was performed using GraphPad Prism 7 software. Statistical parameters including number of mice (n) and number of replicates are described in the figure legends. Data are represented as mean plus or minus SEM. To compare ratios of two

groups, data is presented as % of control and error bars indicate SE of ratio. Analysis of significance between 2 groups of mice was performed using unpaired t-tests unless otherwise specified in the figure legends. For comparison between more than two groups, ordinary one-way analysis of variance (ANOVA) followed by Tukey's test was used unless otherwise specified in the figure legends. $p < 0.05$ was considered as significant. Relative Movement (RM) of cells through the S phase was assessed relative to that of G1 and G2M cells by measuring their mean fluorescence intensity (DNA levels) over time (green dots). RM is calculated with F_L as the mean fluorescence and F_{G1} and F_{G2M} as fluorescence values of G1 and G2M as follows:

$$RM = \frac{F_L - F_{G1}}{F_{G2M} - F_{G1}}$$

Mixtures of Gaussian distributions (Figure 5F) were fitted using the mixdist R package.

Agent-based model

General strategy

in vivo EdU and BrdU labeling is a complex process since cells only receive labeling during the S phase, whose intensity depends on the speed of DNA incorporation (i.e., speed of the S-phase) and the duration of bioactive labeling. Further, mitosis causes a decrease of label intensity and doubles the amount of labeled cells. Therefore, a quantitative mathematical analysis is required. We designed a mathematical model to assess the likelihood *(cost)* of cycle phase durations *(parameters)* to reproduce the experimental kinetics of EdU/BrdU labeling *(observed variables)* as in the presented workflow (Figure 4A). The model simulates a population of dividing cells *(agents)* and returns the expected labeling kinetics under a set of parameter values (in particular, the duration of cell cycle phases). The extent of deviation between simulation and the experimental data-points defines the objective 'cost value' to be minimized. Search heuristics that test large numbers of parameter values, allow finding cell cycle durations generating the minimal cost *(parameter optimization)*, and return the most likely phase durations to explain the experimental dataset. In the model, we simulate a population of dividing cells (the agents). We simulate separately the DN2, DN3a, DN3b, DN4 and pre-selection DPs with their own set of parameters (Table S2). We explain how a simulation is performed from a hypothetical set of parameter values and how cells are updated over time for cell cycling, death and exit.

Cycle phases

The time evolution of the cell cycle is defined by a time-distribution for each possible event. The duration of the G1, S and G2/M phase are defined by three lognormal laws, with mean and standard deviations (in linear scale) named μG_1, σG_1, μS, σS, $\mu G2/M$, $\sigma G2/M$. Phases that are assumed non-variable are modeled with null standard deviation. Death is assumed to happen with a constant rate and therefore follows an exponential distribution of parameter λ. λ can be converted into a death rate δ per hour using $\delta = 1/\lambda$. A cell dies only if its time of death falls before it would perform mitosis. In order to obtain the sample cycle phase durations with lognormal distribution of actual mean μ and standard deviation σ, the following formula were used:

$$\mathrm{distrib}_{G1}, \mathrm{distrib}_{S}, \mathrm{distrib}_{G2M} \sim \mathrm{Lognormal}\left(\ln(\mu) - \frac{1}{2}\ln\left(1 + \frac{\sigma^2}{\mu^2}\right), \sqrt{\ln\left(1+\frac{\sigma^2}{\mu^2}\right)}\right)$$

$$\mathrm{distrib}_{death} \sim \mathrm{Exponential}(\lambda)$$

Cells

Two types of cells are considered. Non-cycling cells contain either quiescent cells that stay in the G0 phase or bystander 'long G1' cells that do not cycle during the time of experiment, while cycling cells can be in G1, S and G2/M phases. Mitosis is included inside the G2 phase because it is fast and hardly distinguishable from G2. During a simulation, each cell carries information about the timing of its own past and future events (Table S3): time of birth (in G1 phase), ending time of each cycle phase, and time of death. A cell is also tagged with its generation and its instant DNA amount (labeled or unlabeled with EdU or BrdU).

Initialization of new cells

When a cell is created *(Algorithm 1,* Data S1*)*, all its events are sampled according to the time-distributions for the cycle phases and death. This assumes independence between cells: that their cell cycle is predefined at birth and is not influenced by dynamical factors such as changes in population size. When daughter cells are created by mitosis, the current time becomes their time of birth, and each following event for both cells are sampled once for all, from the respective death or phase duration distributions. At the start of a simulation, in order to start with a steady-state population of cells in each stages of the cell cycle, cells are generated in the middle of the cell cycle: each event is sampled and shifted to the past, such that the current time falls randomly inside one of the phases proportionally to their duration. Finally, a quiescent cell is created by setting its state to G0 and giving '$+\infty$' as a time point for all phase progression events so they never happen.

Population initialization

A population of size *Ncells* is simulated, with a fraction of non-cycling cells noted *q0*. We assume that EdU or BrdU injections do not significantly alter proliferation during the time frame of the experiment, and that non-cycling cells are constant over time. Previous mathematical models for EdU labeling assumed an exponential population growth without exit,[52–54,61] which is a valid assumption in cell cultures and simplifies the mathematical formulation but might introduce biases in the present case. As in some population

models of thymic development,[62–64] we instead assume the cells stay in a population for an average number of divisions ***Ndiv*** before they exit, coupled with an inflow of unlabeled progenitors to maintain population time. For instance, a value of *Ndiv = 1.6* means that 40% of cells will perform one division whereas 60% perform two divisions, and *Ndiv – floor(Ndiv)* defines the fraction of cells performing one more division.

At equilibrium, each generation contains more cells than the previous generation (provided death is low and the population is expanding between inflow and outflow). Therefore, if a population of cells is generated by uniformly sampling generations among cells, this population is not stable over time. *Algorithm 2* (Data S1) shows how to generate an initial pool of cells with appropriate generations. The function *equilibriumGenerations* calculates the distribution between generations at equilibrium. The average time to complete a full cycle *T* is derived from each cycle phase time distribution, and the death rate δ from the death time distribution. During a period of time *T*, the cells will expand on average 2 times by proliferation and die ***T.***δ (approximation of *1 – exp(-t.* δ*)*, provided death is low). Therefore, the average expansion rate of the population is *X = 2(1- T* δ*)*. The fraction of cells in each generation is calculated knowing that each generation is *X* times bigger than the previous one, and only a fraction of cells enter the last generation. The function GenerateCells then generates a population of *Ncells* cells, either non-cycling (fraction *q0*) or at a random phase of the cycling from *Algorithm 1 (*Data S1*)*, with appropriate generations.

Simulation of a dual pulse labeling

Algorithm 3 (Data S1) explains how the population of cells are updated at each time-step at time *time,* updated every ***dt***, and assuming an instant level of bioavailability of EdU and BrdU. Since each cell contains the information of its future event, each cell ***t*** is checked for its events happening between *time - dt/2* and *time + dt/2.* Death is checked first and leads to cell removal. Alive cells are updated for their DNA level depending on their phase (DNA levels increase linearly from 1 to 2 during the S-phase, Figure 4B). The newly synthesized DNA during this ***dt*** time is labeled proportionally to the current levels of EdU and BrdU (∈ [0,1] each). Phase completion events are performed by changing the cycle state. At the end of the G2/M phase, if ***t*** was not completing its last division, two new daughters are created at G1 with their own new events and an incremented generation compared to the mother cell, ***t***, which is then removed from the simulation. If the two cells are reaching the last possible generation, only with chance *Ndiv – floor(Ndiv)* they will stay and be tagged for exit after the next mitosis, or exit directly (be removed). Finally, a constant inflow of unlabeled cells is calculated as needed to maintain the 'generation 0' constant, ensuring the full population to be constant over time.

Identification of cell phase durations

All parameters necessary to define and perform a simulation are listed in Table S2. Phase durations and width are unknown and 'fitted' by parameter estimation within the given minimum and maximum boundaries, depending on the chosen hypothesis of phase heterogeneity (Figure 4B). The list of fitted variables is shown in Table S4. The fraction of non-cycling cells *q0* is either fitted (simulations with long G1 cells) or taken as a background value of 4% taken as an average value from experimental data. Finally, we chose to simulate 10,000 cells per population for the sake of computational complexity. EdU^+ or $BrdU^+$ cells were defined as cells with more than 0.01 of labeled DNA (on a scale from 0 to 2). We assumed each pulse to be efficient for a duration of 45 min.[65,66]

Each time a simulation is performed (Algorithm 4), the cost function between simulation and data is the Mean Standard Error (MSE) normalized for each curve separately by its average value along all time points, such that each curve has a balanced contribution to the total cost. This assumes that the variance is proportional to the measurements. Due to the low number of mice per time point, we did not include experimental standard deviations inside the cost calculation, as it was putting the weight only on points with low standard deviation by chance, and the fittings were not of good quality. With Nv variables, K time-points, $x_{v,t}$ the measurement and $\overline{x}_{v,t}$ the simulation of variable v at time-point t, the normalized MSE is therefore:

$$\sum_{v=1}^{Nv} \frac{1}{mean(x_v)} \sum_{t=1}^{K} \frac{(x_{v,t} - \overline{x}_{v,t})^2}{K}$$

We have used an evolutionary strategy algorithm as a search heuristic for parameter estimation, using the Moonfit framework in C++.[60] A population of possible parameter sets (individuals) is generated with uniform values within the given unknown parameter boundaries. Each individual also carries a mutation speed on its own for each parameter, and is associated with a fitness, that is, the cost of a labeling simulation performed with its parameters. New individuals are generated by mutation (changing parameter values) or recombination between two parents. Mutation followed a normal distribution sampled for all the parameters independently at the same time. The SBX crossover was used for recombination,[60] sampling of parents was made proportional to their fitness, defined as the competitive advantage relative to the current worst individual fitness. Offspring did not replace the parents, but only the best individuals (including parents and progeny) were kept after each round of mutations and recombination, to maintain the number of individuals. Each optimization was performed ten times separately, using a population of 250 individuals along 100 rounds of generation/selection. Every round, 20% of the population was generated as new individuals by cross-over, while 50% of the population size was generated by mutation. Therefore, one optimization tests 25,000 possible parameter sets, each simulating the labeling of a population of 10,000 cells.

Two-population model

To simulate the effect of inflow of cells from the ancestor population of the main population of interest, the two-populations model simulates the ancestor population with *5 x Ncells* cells and following previously identified cell cycle durations (i.e., none of the ancestor population parameters are part of the fitting). For each time-step dt, the main population requests a certain number of

new inflow cells and picks randomly from the pool of cells that exited the ancestors at this same time-step (which was the reason to simulate a much bigger ancestor population to always have cells available). If not enough cells are available, an inflow deficit accumulates, and more cells are taken in the next time-steps. We have checked that such a deficit never accumulated in the simulations, and 5 x Ncells was sufficient as the ancestor population size. In contrast to the one-population model, where cells were generated at any cycle phase, the ancestor cells only exit after mitosis and therefore always enter at the beginning of their G1 phase, which allows to have a consistency between entry at mitosis and exit at mitosis in the main population. However, we checked that entry at a random cell cycle phase from the ancestors to the main population, gave the exact same identified phase durations (Figure S6C), showing that the phase of entry in a population did not hamper our capacity to identify phase durations.

Prediction of cell cycle modulation after irradiation

To estimate if irradiation had an impact on different phases of the cell cycle, we simulated side-by-side the dual-pulse labeling of control (ctrl) and irradiated (irrad) mice, and optimized the summed cost of both simulations to the respective datasets. Of note, the ctrl dataset was generated together with the irrad dataset and comes from distinct experiments than the kinetic labeling used in the previous figures. Different hypotheses for which cycle phase is impacted by irradiation are considered (Figures S7C and S7D). The null hypothesis ('none') assumes that ctrl and irrad mice have the same cell cycle phase durations and both simulations share all parameters. The 'diff G1', 'diff S', 'diff G2/M' assume only one phase is modulated by irradiation, and both ctrl and irrad simulations share all parameters except the duration of the respective phase. Finally, the 'diff All' condition assumes that all phase durations are impacted by irradiation and the two simulations have independent parameters. The condition in green boxes (Figures S7C and S7D) shows the minimum model complexity that explains the ctrl and irrad datasets with the best cost. In DN3a and pre-selection DPs, a different G1 duration between ctrl and irrad was necessary to explain the data, but not any other phase, suggesting that irradiation only modulated the G1 phase in those two populations. In other populations, a modulation of each phase was necessary to explain the data.

Comparison of model hypotheses using AICc

For each model hypothesis (which cell cycle phase is variable between cells and whether long G1 cells are allowed), we calculated the corrected Akaike Information Criterion (AICc) which compares the cost of the best curve for each hypothesis, giving a penalty to hypotheses with more parameters. The lowest AICc describes the best hypothesis. The AICc is calculated with the following formula, where experimental data is assumed to follow a Gaussian distribution, n represents the amount of independent fitted points ($n = 44$ for 4 time-points and $n = 62$ for 6 time-points), and k is the number of unknown parameters.

$$\mathrm{AIC}_c = -2\ln(L(\boldsymbol{\theta}|\mathrm{data})) + 2\frac{kn}{n-k-1} = C + \sum_{j=1}^{n}\frac{\left(x_{\theta j} - \widehat{\mu}_j\right)^2}{\widehat{\sigma}_j^2} + 2\frac{kn}{n-k-1}$$

Resources needed

On a simple laptop with a Core i7-11370H processor, 16GB RAM, one parameter estimation takes between 4 h and 6 h on a single CPU in the one-population model and 20–24 h for a two-populations model. Most simulations were carried out on Immunohub e-Infrastructure funded by University of Oslo in close collaboration with the University Center for Information Technology, University of Oslo, IT-Department (USIT), build with 2 x AMD EPYC 7742 64-Core Processor on 2038 GiB RAM. In this architecture, a one-population estimation takes 2 h and a two-populations one 8 h, respectively.